

Evaporation and wetting behavior of silver-graphene hybrid nanofluid droplet on its porous residue surface for various mixing ratios

F.R. Siddiqui¹, C.Y. Tso², S.C. Fu³, H.H. Qiu¹, Christopher Y. H. Chao^{3*}

¹Department of Mechanical and Aerospace Engineering, The Hong Kong University of Science and Technology, Hong Kong

²School of Energy and Environment, City University of Hong Kong, Hong Kong

³Department of Mechanical Engineering, The University of Hong Kong, Hong Kong

* Corresponding Author Tel.: +852 3917 2800

E-mail Address: cyhchao@hku.hk

Postal Address: Department of Mechanical Engineering, The University of Hong Kong, Pokfulam Road, Hong Kong

Abstract

Droplet evaporation has a high heat removal capacity and widely used in the form of spray cooling or dropwise cooling of various heat dissipating devices. However, due to the limiting heat flux removal capacity of conventional fluids, such as water, these cannot be used in thermal management of high heat flux devices. In this research, the evaporation of silver (Ag)-graphene (GNP) hybrid nanofluid droplet and its residue effects on the evaporation of subsequent Ag-GNP hybrid nanofluid droplet, due to its synergistic thermal properties, is experimentally investigated for various mixing ratios, from MR-1 (0.1(Ag):0.9(GNP)) to MR-5 (0.9(Ag):0.1(GNP)), and different residue sizes. A theoretical model is also proposed for hybrid nanofluid droplet evaporation and semi-empirical relations are developed to estimate the hybrid nanofluid droplet spreading over its residue surface. The results show a substantial increase in the droplet evaporation rate with increasing residue size and decreasing mixing ratio. MR-1 hybrid nanofluid droplet gives the highest evaporation rate (up to 370%) on its highly wetted residue surface, while the evaporation rate significantly drops moving from MR-2 to MR-5 hybrid nanofluid droplets on their partially wetted residue surfaces. Moreover, the evaporation rate substantially increases (up to 240%) with increasing residue size for MR-1 hybrid nanofluid droplet resting on its residue

31 surface, however, the effect of residue size on droplet evaporation rate considerably diminishes
 32 moving from MR-2 to MR-5 hybrid nanofluid droplets resting on their respective residues.

33 **Keywords:** Droplet evaporation; wetting; hybrid nanofluid; porous residue; droplet spreading.

34

35 **Nomenclature**

A_s	Droplet surface area, m^2	V_{sd}	Volume of second droplet, μl
a_p	Areal porosity	V_{as}	Droplet volume above residue surface, μl
C	Total molar concentration, $kmolm^{-3}$	V_{bs}	Droplet volume below residue surface, μl
D	Mass diffusivity, m^2s^{-1}	V_{net}	Net droplet volume, μl
\dot{E}_{ins}	Instantaneous evaporation rate, μls^{-1}	x_v	Vapor mole fraction
\dot{E}_{net}	Net evaporation rate, μls^{-1}	Greek Letters	
\dot{E}''_{ins}	Instantaneous evaporation flux, $\mu ls^{-1}m^{-2}$	ρ	Density, kgm^{-3}
g	Gravitational constant, ms^{-2}	γ_{lv}	Droplet surface tension, mNm^{-1}
h	Height, m	γ_{sv}	Surface free energy, mNm^{-1}
h_c	Characteristic height, m	γ_{sl}	Solid-liquid interfacial tension, mNm^{-1}
l_{ca}	Capillary length, m	φ	Relative humidity
M	Molar mass, g/mol	θ_{qe}	Quasi-equilibrium contact angle
MR	Mixing ratio	θ_d	Dynamic contact angle
P_a	Ambient Pressure, Pa	θ_s	Static contact angle
$P_{v,sat}$	Saturation vapor pressure, Pa	θ_y	Young contact angle
r	Roughness ratio	θ_a	Apparent contact angle
R_a	Average surface roughness, μm	\emptyset_{qe}	Quasi-equilibrium contact diameter, m
R	Universal gas constant, $Jmol^{-1}K^{-1}$	\emptyset_d	Dynamic contact diameter, m
T	Temperature, K	\emptyset_s	Static contact diameter, m
t	Time, s	\emptyset_f	Mean Feret diameter, m
VES	Vapor equilibrium surface	τ	Droplet spreading time scale, s
V_{fd}	Volume of first droplet, μl	μ	Viscosity, Pas

36 **1. Introduction**

37 Droplet evaporation is a universal phenomenon and finds a range of engineering applications such
38 as spray cooling, printing, spray painting, fuel injection, and hotspot cooling in microelectronics.
39 It is a phase change process with higher heat transfer rates as compared to the single-phase heat
40 transfer processes. The evaporating droplet removes heat by utilizing the latent energy of its
41 molecules until it transforms into a vapor. Despite all these advantages, thermal management of
42 high heat flux devices (10^6 - 10^7 W/m²) [1] is increasingly becoming a challenge thus limiting the
43 use of conventional fluids (such as water) for such applications. Therefore, advanced thermal
44 fluids, such as nanofluids with high heat removal capacity, are needed to address such challenges.

45

46 Nanofluid is the dispersion of very fine nano-sized particles in the base fluid (such as water), which
47 substantially improves its thermal properties and is widely reported by researchers [2–4].
48 However, nanofluids do not possess overall hydrothermal properties, such as high stability and
49 high thermal conductivity. For instance, metal (such as copper) nanofluids show high thermal
50 conductivity but poor dispersion stability. On the other hand, metal-oxide (such as Al₂O₃)
51 nanofluids exhibit high dispersion stability but low thermal conductivity. Due to this reason, single
52 particle nanofluids are not suitable for heat transfer applications as they do not possess overall
53 hydrothermal characteristics [5]. Recently, another class of nanofluid (known as the hybrid
54 nanofluid) is investigated, which has resulted in better overall hydrothermal properties and is
55 prepared by dispersing two different nanoparticle types (metal, metal-oxide or non-metal) in the
56 base fluid. Also, the presence of two different nanoparticle types has a synergistic thermal effect,
57 thus making the hybrid nanofluid a highly conductive fluid, which is not the case with single
58 particle nanofluid. At even low particle concentration, hybrid nanofluids are reported to exhibit
59 higher thermal conductivity than single particle nanofluids [6–9]. The synergistic thermal
60 conductivity in the hybrid nanofluid is due to a thermal pathway created by one nanoparticle type
61 with another nanoparticle type, thus reducing the overall thermal contact resistance between the
62 nanoparticles and the surrounding molecules of the base fluid [10]. For this reason, the synergistic
63 thermal effect in hybrid nanofluid highly depends on the inter-particle compatibility. It is the
64 synergistically advanced thermal properties of the hybrid nanofluid that makes it a suitable
65 candidate for thermal management of high heat flux applications.

66

67 The application of hybrid nanofluid in a phase change process, such as droplet evaporation, may
68 result in a high heat removal rate and keep the surface temperatures within safe levels. There are
69 several parameters that affect the evaporation rate of a sessile droplet such as the surface
70 temperature, humidity, surface roughness and droplet surface tension, to name a few [11–13].
71 Besides, the droplet pinning or de-pinning effect over the substrate also affects its evaporation rate
72 [14,15]. As reported by many researchers, the suspended nanoparticles in the nanofluid droplet
73 migrate towards the edge and deposit near the three-phase contact line, which results in a droplet
74 pinning effect during the evaporation process [16–21]. Other factors, such as the droplet contact
75 angle, viscosity, and suspended nanoparticle type and concentration also influence the droplet
76 evaporation rate [22–25]. Approximate solutions have also been developed to predict the
77 evaporation rate of sessile droplets [26–28]. Moreover, the suspended nanoparticles in the sessile
78 nanofluid/hybrid nanofluid droplet do not apparently improve the evaporation process, when all
79 the three phases (droplet, solid substrate and the air) are in thermal equilibrium [14,21].

80
81 During evaporation, the concentration of suspended nanoparticles in the hybrid nanofluid droplet
82 increases with time, and finally deposit over the substrate to form a nanostructured porous residue
83 surface. Although, many researchers have reported the formation of different residue patterns as a
84 result of nanofluid or hybrid nanofluid droplet evaporation [29–32], there is still a lack of research
85 on how the deposited residue affects the evaporation rate of the subsequent hybrid nanofluid
86 droplet resting on its surface formed by the first evaporating hybrid nanofluid droplet. This
87 phenomenon may be highly relevant to hybrid nanofluid based spray cooling or dropwise cooling
88 applications, where the residue formed by the first evaporating hybrid nanofluid droplet may
89 improve the evaporation rate of the subsequent hybrid nanofluid droplets, and thus may have a
90 higher cooling effect in such applications.

91
92 In our previous study [14], we have shown that the deposited residue substantially improves the
93 wetting properties of the copper substrate. This tremendously increases the evaporation rate
94 (~163-196%) of the subsequent hybrid nanofluid droplet resting on the residue surface as
95 compared to the pure copper surface. Also, high surface wettability of the deposited residue
96 improves spreading dynamics of the subsequent hybrid nanofluid droplet, resulting in large liquid-
97 vapor interfacial area and high evaporation rates. Moreover, the suspended nanoparticles increase

98 disjoining pressure near the droplet edge, thus improving droplet spreading over the substrate [33–
99 35]. Droplet spreading, which affects the evaporation rate of subsequent droplet over the residue
100 surface, is divided into three main regimes, the inertial spreading regime (high inertial forces), the
101 capillary spreading regime (high capillary forces) and the gravitational spreading regime
102 (gravitational forces affect spreading) [36].

103

104 This study aims to investigate the evaporation rate of the Ag-GNP hybrid nanofluid droplet on two
105 different types of surfaces, i.e. a pure copper surface and a residue surface formed by the
106 evaporation of first Ag-GNP hybrid nanofluid droplet. It is a well-known fact that nanofluid or
107 hybrid nanofluid droplet leaves behind a residue on the substrate at the end of evaporation [29–
108 32]; however, there is no study to date on how this residue affects the wettability and evaporation
109 rate of the subsequent hybrid nanofluid droplet that sits over the residue surface. The deposited
110 residue may transform the substrate into a highly wetted surface, which may improve the spreading
111 and evaporation rate of the subsequent droplet resting on it. Besides having a synergistic thermal
112 conductivity of the Ag-GNP hybrid nanofluid droplet, which may result in high evaporation rates,
113 its droplet residue also plays a key role, which is to further enhance the evaporation rate of the
114 subsequent Ag-GNP hybrid nanofluid droplet resting on its surface. Therefore, the evaporation
115 rate of the subsequent Ag-GNP hybrid nanofluid droplet is investigated for various residue sizes,
116 resulting from the evaporation of first Ag-GNP hybrid nanofluid droplet. Moreover, this study also
117 highlights the fundamental underlying mechanisms that affect the hybrid nanofluid droplet
118 evaporation rate, such as the wetting characteristics, spreading dynamics and residue surface
119 properties.

120

121 The main novelty of this research is to study the effect of the Ag-GNP hybrid nanofluid mixing
122 ratio on droplet evaporation rate. The droplet wetting characteristics, as well as the residue surface
123 properties, vary considerably with the varying mixing ratio, which eventually affects the droplet
124 evaporation rate. Therefore, the proposed research is focused to determine the Ag-GNP hybrid
125 nanofluid mixing ratio which gives the highest evaporation rate on its respective residue surface.
126 Another novel aspect of proposed research is the manipulation of subsequent hybrid nanofluid
127 droplet wetting characteristics (contact angle and contact diameter), based on the residue size of
128 first evaporated hybrid nanofluid droplet. Droplet wetting manipulation can be important for

129 applications, such as the dropwise hotspot cooling in microelectronics, where the residue size of
130 the first evaporated hybrid nanofluid droplet can be used to manipulate the contact angle and,
131 eventually, the evaporation rate of the subsequent hybrid nanofluid droplet. Based on the above
132 discussion, the main objectives of this research are as follows:

133

- 134 • To study the effect of Ag-GNP hybrid nanofluid mixing ratio on droplet evaporation rate;
- 135 • To study the effect of residue size, resulting from the evaporation of first hybrid nanofluid
136 droplet, on the evaporation rate of the subsequent hybrid nanofluid droplet;
- 137 • To identify the residue surface properties that affect the droplet evaporation rate.

138

139 **2. Experimental Methodology**

140 In this section, we firstly discuss the experimental techniques that were used in the synthesis of
141 the Ag-GNP hybrid nanofluid. Later, we discuss the methodology that we used to study the droplet
142 evaporation, droplet spreading, and wetting and residue characterization of the Ag-GNP hybrid
143 nanofluid.

144

145 **2.1. Hybrid Nanofluid Synthesis**

146 The Ag-GNP hybrid nanofluid was prepared by a two-step method, in which Ag and GNP
147 nanoparticles were dispersed in water, pre-treated and then ultra-sonicated for two hours [37]. **A**
148 **detailed procedure for synthesis of the Ag-GNP hybrid nanofluid and criteria for selecting this**
149 **combination (Ag-GNP) in proposed research is discussed in our previous study [14].** Both, GNP
150 (carbon>70% and oxygen>10% by weight, polycarboxylate functionalized) and Ag (particle
151 size<100nm, polyvinylpyrrolidone) nanoparticles were purchased from Sigma Aldrich and the
152 prepared Ag-GNP hybrid nanofluid samples were found stable for several hours. The Ag-GNP
153 hybrid nanofluid was prepared at a fixed particle concentration of 0.1% volume fraction (as the
154 particle concentration effect on the droplet evaporation rate was not the main focus of our research)
155 and various mixing ratios (as shown in Table 1). The droplet evaporation rate and its residue
156 wetting behavior for the Ag-GNP hybrid nanofluid was investigated **and compared with Ag and**
157 **GNP nanofluids**, as discussed in the following sub-section 2.2.

2.2. Droplet Evaporation, Spreading and Wetting Measurements

In this section, we first discuss the experimental technique that we used to study the Ag-GNP nanofluid/hybrid nanofluid droplet evaporation and wetting characteristics (contact angle and contact diameter) over the residue surface, formed by the evaporation of first Ag-GNP nanofluid/hybrid nanofluid droplet. In the second part, we discuss the same experimental technique but with slightly different settings, to study the spreading behavior of the subsequent Ag-GNP nanofluid/hybrid nanofluid droplets over their respective residue surfaces.

The experimental setup and procedure to measure the droplet evaporation rate and wetting characteristics (such as the contact angle and contact diameter) using an optical tensiometer is explained in detail in our previous study [14]. The main advantage of using an optical tensiometer is that the droplet volume, along with its wetting properties, can be measured at each time step. The temperature inside the test section of tensiometer was kept the same as the room temperature $T=22\text{ }^{\circ}\text{C}$, to keep all the three phases (droplet, substrate and air) at thermal equilibrium. Wet air, at an extremely low flow rate (to minimize the advection effects), was introduced into the environmental chamber covering the test section of the tensiometer to maintain the relative humidity fixed at $\varphi=0.3$, in all our experiments. The reason to keep a low relative humidity of $\varphi=0.3$ in our experiments was to reduce the droplet evaporation time, as droplets take more time to evaporate at high humidity values. As the humidity effect on droplet evaporation rate was not the main focus of our research, therefore, it was fixed at $\varphi=0.3$ in all our experiments. The droplet images during the evaporation process were recorded at 14 frames per second. The measurements for Ag-GNP nanofluid/hybrid nanofluid droplet evaporation and wetting properties follow a two-step process as discussed by Siddiqui et al. [14]. We used four different droplet volume ratios (V_{fd}/V_{sd}) as 1, 5, 10 and 20 in our experiments, where we fixed the volume of the second droplet as $V_{sd}=3\mu\text{l}$, while only the volume of the first droplet (V_{fd}) was increased to allow spreading of the second droplet onto the residue developed by the first droplet. We performed each experiment three times at different locations on the copper surface.

The droplet evaporation and wetting experiments were followed by the experiments on spreading dynamics of the Ag/GNP nanofluid/hybrid nanofluid droplets over their respective residue surfaces, by using the same optical tensiometer technique. The residue samples were prepared by

189 following the same two-step process [14] as used in the droplet evaporation experiments. However,
190 due to the fast spreading dynamics, which only lasted for a few seconds, the droplets were recorded
191 at a high frame rate of 28 frames per second. The tensiometer video camera recorded the droplet
192 images as it came out of the dispenser until it reached a quasi-equilibrium state (droplet spreading
193 ends macroscopically). The experimental techniques used in residue characterization are discussed
194 in the following sub-section 2.3.

195

196 **2.3. Residue Measurements**

197 The porous structure of the Ag-GNP nanofluid/hybrid nanofluid droplet residues were
198 characterized by using a scanning electron microscope (TM 3030, Hitachi, Japan). Each
199 measurement was performed three times at different locations on a residue surface, using 3000x
200 magnification. The micrographs were post-processed using an ImageJ software, in order to
201 determine the pore size (Feret diameter) and residue areal porosity, with a maximum mean
202 standard deviation of 0.135 μm and 2.3%, respectively. The roughness parameters (surface
203 roughness (R_a) and roughness ratio (r)) of droplet residues were measured by using an optical
204 profiler (NPFLEX, Bruker, USA), with a maximum mean standard deviation of 0.26 μm . A 10x
205 objective and a green light for illumination were used during the surface roughness measurements.
206 The surface free energy (γ_{sv}) of each droplet residue was measured on an optical tensiometer, by
207 using a polar fluid (water) and a dispersive fluid (diiodomethane) based on OWRK/Fowkes model
208 [38], with a maximum mean standard deviation of 1.7mN/m. Also, the droplet surface tension (γ_{lv})
209 and its solid-liquid interfacial tension (γ_{sl}) were measured using an optical tensiometer.

210

211 **3. Theoretical Modelling of Ag-GNP Nanofluid/Hybrid Nanofluid Droplet Evaporation on** 212 **its Porous Residue Surface**

213 A theoretical model is developed to estimate the instantaneous evaporation rate of the subsequent
214 Ag-GNP nanofluid/hybrid nanofluid droplet over the residue surface developed by the first
215 evaporated Ag-GNP nanofluid/hybrid nanofluid droplet. The schematics of the Ag-GNP
216 nanofluid/hybrid nanofluid droplet over its respective residue surface is shown in Fig. 1(a). The
217 droplet height is denoted as h_1 , while the height of the vapor equilibrium surface (VES) is denoted
218 as h_2 , as illustrated in Fig. 1(a). The vapor equilibrium surface (VES) is the hypothetical surface
219 above the droplet, where the vapor concentration is in equilibrium with the ambient conditions,

220 i.e., $x_{v,2} = \varphi_2 x_{v,1}$ where $\varphi_2=0.3$. Moreover, fully saturated vapor conditions ($x_{v,1} = P_{v,sat}/P_a$)
 221 are assumed at the droplet-air interface, while the air-vapor mixture above the droplet is assumed
 222 as an ideal gas.

223 As both the droplet and the substrate are at room temperature and all the three phases (droplet,
 224 substrate and air) are at thermal equilibrium in this study, the proposed evaporation model is based
 225 on Fick's Law of mass diffusion and isothermal steady-state assumption. Although wet air (at
 226 extremely low flow rate) was induced inside the environmental chamber to control humidity in our
 227 experiments, the stationary medium approximation [39] is considered in the proposed model with
 228 negligible advection effects. Based on our experimental observation, only droplet height varies,
 229 while the contact diameter remains constant (pinning effect) during droplet evaporation. Therefore,
 230 one-dimensional diffusion along the height (h) is assumed in our model, as shown in Fig. 1 (b).
 231 Furthermore, all droplets are assumed as spherical caps (negligible gravitational effect), since the
 232 contact radius remains within the capillary length ($l_{ca} = \sqrt{\gamma_{lv}/\rho g}$) during droplet spreading over
 233 the residue surface. As the droplet size is larger than the residue surface roughness by 2-3 orders
 234 of magnitude in our proposed study, Wenzel approximation [40] holds and the nanofluid/hybrid
 235 nanofluid droplet is assumed to completely fill the pores underneath it. The evaporation model is
 236 developed based on three input parameters as the droplet height (h_l), quasi-equilibrium contact
 237 diameter (Φ_{qe}) and the vapor concentration gradient dx_v/dh . The instantaneous droplet
 238 evaporation flux \dot{E}''_{ins} ($\mu l/s.m^2$) is determined as [39]:

$$239 \quad \quad \quad 240 \quad \quad \quad \dot{E}''_{ins} = \frac{-MCD}{\rho} \left(\frac{dx_v}{dh} \right), \quad (1)$$

241
 242 and the instantaneous droplet evaporation rate \dot{E}_{ins} ($\mu l/s$) is given as:

$$243 \quad \quad \quad 244 \quad \quad \quad \dot{E}_{ins} = \frac{-MCD}{\rho} \left(\frac{dx_v}{dh} \right) A_s, \quad (2)$$

245 where M , C , D , ρ and A_s are the molar mass of water (g/mol), total molar concentration of air-
 246 vapor mixture (mol/m³), mass diffusivity of vapor into the air (m²/s), water density (kg/m³) and
 247 the droplet-air interfacial area (m²), respectively. dx_v/dh is the vapor concentration gradient
 248 between the droplet-air interface ($x_v = x_{v,1}$) and the vapor equilibrium surface ($x_v = x_{v,2}$), as
 249

250 shown in Fig. 1(a). The total molar concentration of air-vapor mixture (C) above the droplet is
 251 determined from the ideal gas law as:

$$252 \quad C = P_a/RT, \quad (3)$$

254 where P_a and T are the ambient pressure and temperature as 101.325 kPa and 22 °C (room
 255 temperature), respectively, and R is the universal gas constant ($R=8.314$ J/molK). Since $A_s =$
 256 $\pi[(\phi_{qe}/2)^2 + h_1^2]$, equation (2) can be written as:

$$257 \quad \dot{E}_{ins} = k \left(\frac{dx_v}{dh} \right) [(\phi_{qe}/2)^2 + h_1^2], \quad (4)$$

258
 259 where $k = -\pi MCD/\rho$ is a constant, ϕ_{qe} (m) is the quasi-equilibrium contact diameter (contact
 260 diameter at an instant when droplet spreading ends macroscopically) and h_l (m) is the droplet
 261 height. The unknowns in equation (4) are ϕ_{qe} , h_1 and dx_v/dh and, therefore, we need to develop
 262 relations for each of these unknowns. We first develop a relation to determine the quasi-
 263 equilibrium contact diameter (ϕ_{qe}) for considered nanofluid/hybrid nanofluid droplets. Although
 264 we have measured ϕ_{qe} in our experiments, we further develop a relation based on the Young
 265 equation and droplet geometry, and subsequently compare the theoretical and measured values of
 266 ϕ_{qe} (see Fig. 4(c)). The droplets studied in proposed research exhibit different quasi-equilibrium
 267 contact diameters, due to their different surface tensions as well as varying surface chemistry, and
 268 surface roughness of their corresponding residues. The Young equation is given as [41]:
 269
 270

$$271 \quad \theta_y = \cos^{-1} \left(\frac{\gamma_{sv} - \gamma_{sl}}{\gamma_{lv}} \right), \quad (5)$$

272
 273 where θ_y is the Young contact angle and γ_{sv} , γ_{sl} and γ_{lv} are the interfacial tensions at the three-
 274 phase contact line of a sessile droplet. Based on the Wenzel effect [42], we get:
 275
 276

$$277 \quad \theta_{qe} = \cos^{-1}(r \cos \theta_y), \quad (6)$$

278

279 where r is the roughness ratio and θ_{qe} is the contact angle at a quasi-equilibrium state. The
 280 measured values for r , θ_a and interfacial tensions (γ_{sv} , γ_{sl} and γ_{lv}) for Ag-GNP nanofluid/hybrid
 281 nanofluid droplets and their respective residue surfaces are given in Table 1. It should be noted
 282 that θ_{qe} is the theoretical contact angle, while θ_a is the measured or apparent contact angle at a
 283 quasi-equilibrium state. The quasi-equilibrium contact angle (θ_{qe}) from equation (6) is used to
 284 determine the quasi-equilibrium contact diameter (ϕ_{qe}), as given by the following spherical-cap
 285 equation:

$$286 \quad \phi_{qe} = \left(\frac{24V_{as} \sin \theta_{qe} (1 + \cos \theta_{qe})}{\pi(2 + \cos \theta_{qe})(1 - \cos \theta_{qe})} \right)^{1/3} . \quad (7)$$

288 where V_{as} is the droplet volume above the residue surface. It should be noted that equation (7) is
 289 only applicable for unbounded residue surfaces, where the droplet spreading is not restricted by
 290 the residue boundaries. For cases, where the droplet contact diameter is the same as the residue
 291 diameter (completely wetted residue), ϕ_{qe} is considered equal to the residue diameter. As the
 292 droplet spreads over the residue surface, it fills the pores underneath it and, therefore, the net
 293 droplet volume ($V_{net}=3\mu\text{l}$) is equal to the sum of the droplet volume above the residue surface
 294 (V_{as}) and the droplet volume below the residue surface (V_{bs}). The droplet volume above the residue
 295 surface is given as:

$$296 \quad V_{as} = V_{net} - V_{bs} , \quad (8)$$

297 The droplet volume below the residue surface is determined as:

$$298 \quad V_{bs} = \pi a_p R_a (\phi_{qe}/2)^2 . \quad (9)$$

299 where a_p and R_a are the areal porosity and average surface roughness of the droplet residue
 300 respectively, and their measured experimental data is shown in Table 2. Since the variation in
 301 droplet volume above the residue surface (V_{as}) occurs due to evaporation, as well as the droplet
 302 entrainment into the residue pores during the droplet spreading process, the droplet evaporation
 303 rate is determined in the interval when the droplet reaches a quasi-equilibrium state (droplet

309 spreading ends at macroscopic scale), until the end of the evaporation process. Another unknown
 310 term in the equation (4) is the droplet height (h_1), which is determined from the spherical-cap
 311 geometry as:

$$312$$

$$313 \quad h_1 = \sqrt{\frac{\phi_{qe}^2}{2(1+\cos\theta_s)} - \frac{\phi_{qe}^2}{4}} . \quad (10)$$

314 where θ_s is the static contact angle and this varies with time during the droplet evaporation process
 315 (see Fig. 5). We have determined relations for two unknown terms (ϕ_{qe}, h_1) of equation (4) and
 316 now we determine a relation for term dx_v/dh . An empirical model is developed to estimate the
 317 term dx_v/dh , as a function of the static contact angle, mixing ratio and V_{fd}/V_{sd} , by using our
 318 experimental data. The non-dimensional form of this equation is given as:

$$319$$

$$320$$

$$321 \quad \frac{A}{h_c} \frac{dx_v}{dh} = B f\left(\theta_s, MR, \frac{V_{fd}}{V_{sd}}\right) , \quad (11)$$

322 where A and B are the equation coefficients and h_c is the characteristic height equal to A/B . As
 323 both A and B are equal to unity, $h_c = 1\text{mm}$. Thus, ϕ_{qe}, h_1 and dx_v/dh from equations (7), (10) and
 324 (11) are used in equation (4) respectively, to determine the instantaneous evaporation rate of all
 325 studied droplets. It must also be noted, that in equation (4), both ϕ_{qe} and h_1 are the theoretical
 326 values, while dx_v/dh is obtained from the empirical model as discussed in the supplementary
 327 material. The height (h_2) of the vapor equilibrium surface (VES) can be determined from Equation
 328 (11) as:

$$329$$

$$330$$

$$331 \quad x_{v,2} - x_{v,1} = f\left(\theta_s, MR, \frac{V_{fd}}{V_{sd}}\right) h_c (\tilde{h}_2 - \tilde{h}_1) , \quad (12)$$

$$332$$

$$333 \quad h_2 = \tilde{h}_2 h_c = \left(\frac{x_{v,2} - x_{v,1}}{f\left(\theta_s, MR, \frac{V_{fd}}{V_{sd}}\right)} \right) + h_1 . \quad (13)$$

334

335 4. Results and Discussion

336 This section is divided into three main parts. In the first part, the evaporation rate of all considered
337 nanofluid and hybrid nanofluid droplets for various droplet volume ratios (V_{fd}/V_{sd}) is discussed.
338 The second part includes discussion on main factors that affect the droplet evaporation rate, such
339 as the wetting behavior of the nanofluid/hybrid nanofluid droplets on their respective residue
340 surfaces. The droplet spreading dynamics over the residue surface is considered, followed by the
341 discussion on wetting behavior, at both the quasi-equilibrium state and during the droplet
342 evaporation process. The last part is focused on the residue characterization, in which the surface
343 chemistry, porosity and roughness parameters are analyzed, in order to understand how these
344 parameters affect the droplet evaporation rate.

345

346 4.1. Droplet Evaporation Rate

347 The net evaporation rate of the Ag/GNP nanofluid and hybrid nanofluid droplets on various
348 substrates is illustrated in Fig. 2(a). The results show that the droplet evaporation rate is almost the
349 same for all mixing ratios when copper is used as a substrate. However, the net evaporation rate
350 varies remarkably, depending on the hybrid nanofluid mixing ratio and the droplet residue size
351 (i.e., V_{fd}/V_{sd}). It is observed that the net evaporation rate is increased by about 4 times, as V_{fd}/V_{sd} is
352 increased from 1 to 20 in GNP nanofluid and MR-1 hybrid nanofluid droplets. However, the effect
353 of V_{fd}/V_{sd} on evaporation rate starts diminishing, moving from MR-2 to MR-5 hybrid nanofluid
354 droplets, until we reach the Ag nanofluid droplet. For the Ag nanofluid droplet, the residue size
355 has an inverse effect on the droplet evaporation rate. That is, the evaporation rate decreases with
356 an increasing value of V_{fd}/V_{sd} . The main reason for anomalous evaporation rate of the Ag nanofluid
357 droplet is the increase in surface roughness with increasing residue size, which consequently
358 increases the non-wetting characteristics of the residue surface (Wenzel effect [42]), as further
359 discussed in sub-section 4.2. It is also shown in Fig. 2(a) that the evaporation rate is considerably
360 increased for GNP nanofluid and MR-1 to MR-3 hybrid nanofluid droplets, residing on their
361 respective residue surfaces (for $V_{fd}/V_{sd} \geq 5$), as compared to that on the copper surface.

362

363 Fig. 2(b) shows a linear relationship between the net droplet evaporation rate and the quasi-
364 equilibrium interfacial surface area, for all considered nanofluid/hybrid nanofluid droplets.
365 Furthermore, the net droplet evaporation rate decays as a power law function of the quasi-

366 equilibrium contact angle, as shown by the inset in Fig. 2(b). This shows that large quasi-
367 equilibrium contact angle and small quasi-equilibrium interfacial surface area leads to low droplet
368 evaporation rate. The variation in droplet height (h_1) and VES height (h_2) with the residue size
369 (V_{fd}/V_{sd}) of the Ag-GNP nanofluid/hybrid nanofluid droplets, at a quasi-equilibrium state is shown
370 in Fig. 2(c). It is noticed that the droplet height (h_1) is considerably reduced (by about 4 times), as
371 V_{fd}/V_{sd} is increased from 1 to 20 for GNP nanofluid and MR-1 hybrid nanofluid droplets. The VES
372 is also shifted downwards with decreasing droplet height (h_1), however, the difference between h_1
373 and h_2 grows substantially with increasing values of V_{fd}/V_{sd} . This is because the VES height (h_2) is
374 not considerably affected by the variation in the droplet height (h_1). Moreover, V_{fd}/V_{sd} has a
375 reduced effect on the droplet height (h_1) and the VES height (h_2), as we move from MR-2 to MR-
376 5 hybrid nanofluid. Conversely, for the Ag nanofluid, the droplet height (h_1) increases as V_{fd}/V_{sd} is
377 increased, which consequently increases the VES height (h_2). The main reasons for varying droplet
378 height (h_1), with increasing values of V_{fd}/V_{sd} , are discussed in the next sub-section 4.2.

379
380 The variation in volume with time during the course of Ag-GNP nanofluid/hybrid nanofluid
381 droplet evaporation is presented in Fig. 3. The volume is normalized with respect to the initial
382 droplet volume (V_i) at a quasi-equilibrium state, while the time is normalized with respect to the
383 total evaporating time (t_f) for each droplet on the Cu surface. The main reason for normalizing time
384 with respect to the Cu surface is to compare the total droplet evaporation time on each residue
385 surface with that on the Cu surface. It is noticed that the total evaporation time on Cu surface and
386 residue surface with $V_{fd}/V_{sd}=1$ is almost the same for all studied nanofluid/hybrid nanofluid
387 droplets. However, the evaporation time is significantly reduced, as V_{fd}/V_{sd} is increased from 5 to
388 20 for GNP nanofluid and MR-1 hybrid nanofluid droplets. Furthermore, V_{fd}/V_{sd} has a reduced
389 effect on the total evaporation time, moving from MR-2 to MR-5 hybrid nanofluid droplets.
390 Conversely, the evaporation time of the Ag nanofluid droplet on its residue surface is higher than
391 that on the Cu surface. It is noticed that the theoretical results obtained from equation (4) agree
392 well with the experimental data, as illustrated in Fig. 3. The main factors responsible for different
393 evaporation rates of Ag-GNP nanofluid/hybrid nanofluid droplets are discussed in the following
394 sub-section 4.2.

395

4.2. Spreading Dynamics and Wetting Characteristics

The spreading dynamics and wetting behavior of the studied nanofluid/hybrid nanofluid droplets, over their respective residue surfaces, play a key role in the net droplet evaporation rate. This is because the evaporation rate depends on the droplet-air interfacial area, which in turn depends on the droplet spreading and wetting behavior over the residue surfaces. This section is divided into three main parts. In the first part, the spreading dynamics of the nanofluid/hybrid nanofluid droplets over their respective residue surfaces is discussed. The second part is focused on wetting behavior at a quasi-equilibrium state, when the droplet spreading ends at the macroscopic scale. In the last part, the variation in the static contact angle and contact diameter, induced by the droplet evaporation, is discussed for all considered droplets.

Fig. 4(a) and (b) shows the spreading dynamics of Ag-GNP nanofluid/hybrid nanofluid droplets over their respective residue surfaces at $V_{fd}/V_{sd}=20$. It must be noted that the spreading nanofluid/hybrid nanofluid droplets do not reach their residue boundaries at $V_{fd}/V_{sd}=20$. Therefore, the droplet spreading remains unbounded, and is only affected by the residue surface properties and interfacial tensions at the three-phase contact line. It is noticed that all droplets initially undergo a very high spreading rate in the inertial regime (first few points in Fig. 4(a) and (b)), which is followed by the capillary regime, in which the capillary forces overcome inertial forces, until we reach a quasi-equilibrium state. As shown in Fig. 4(a) and (b), GNP nanofluid and MR-1 hybrid nanofluid droplets show significant spreading, due to highly wetted surfaces, resulting from high roughness (r) and surface free energy of their respective residues (Table 1). Such a rapid spreading over highly wetted residue surfaces results in a large droplet-air interfacial area, which substantially improves the droplet evaporation rate. Despite having relatively low surface tension for MR-2 to MR-5 hybrid nanofluid droplets (Table 1), the droplet spreading is reduced, due to the low surface roughness and surface free energy of their residues. On the other hand, the Ag nanofluid droplet spreads inwardly in the inertial regime (as shown in the inset of Fig. 4(a)) due to its non-wetted residue, and quickly attains a quasi-equilibrium state, as compared to other droplets. As the spreading is in the outward direction for GNP nanofluid and MR-1 to MR-5 hybrid nanofluid droplets, a semi-empirical asymptotic relation is developed, to estimate the dynamic contact diameter (\varnothing_d) as a function of spreading time (t), and given as:

427
$$\Phi_d = \Phi_{qe} \left(1 - e^{-\frac{t}{\tau}}\right)^n, \quad (14)$$

428
 429 where τ is the droplet spreading time scale to reach a quasi-equilibrium state and includes both the
 430 initial inertial spreading and the subsequent capillary spreading regimes and given as:

431
 432
$$\tau = \frac{\pi^7 \mu V_{as}^{4/3}}{\gamma_{lv} R_a \Phi_{qe}^2}. \quad (15)$$

433
 434 For the Ag nanofluid droplet, spreading is in the inward direction, due to a highly non-wetted
 435 residue surface, and the dynamic contact diameter ($\Phi_{d,Ag}$) is estimated by the following semi-
 436 empirical relation:

437
 438
$$\Phi_{d,Ag} = \Phi_{qe} \left(1 + e^{-\frac{t}{\tau}}\right)^n, \quad (16)$$

439 where,

440
 441
$$\tau_{Ag} = \frac{\mu V_{as}^{4/3}}{\gamma_{lv} R_a \Phi_{qe}^2}. \quad (17)$$

442
 443 where n is equal to 0.1, 0.033, 0.034, 0.011, 0.133, 0.055 and 0.042 for GNP nanofluid, MR-1
 444 hybrid nanofluid, MR-2 hybrid nanofluid, MR-3 hybrid nanofluid, MR-4 hybrid nanofluid, MR-5
 445 hybrid nanofluid and Ag nanofluid droplets. The semi-empirical equations (15) and (17),
 446 pertaining to the droplet spreading time scale, were developed using the experimental data. It is
 447 noticed in Fig. 4(a) that the droplet spreading time scale (τ) is increased, as we move from GNP
 448 nanofluid to MR-5 hybrid nanofluid, followed by a very low value of τ for Ag nanofluid. Such a
 449 low value of droplet spreading time scale for the Ag nanofluid droplet is also evident from the
 450 experimental data shown in Fig. 4(a), in which the droplet after a short inertial regime (shown in
 451 the inset) quickly gains a quasi-equilibrium state. The dynamic contact angle (θ_d) of spreading
 452 droplets, at any instantaneous time (t), is determined by solving an implicit equation for a
 453 spherical-cap, with known values of V_{as} (equation (8)) and Φ_d (equations (14) and (16)), and given
 454 as:
 455
 456

$$3V_{as}\sin\theta_d(\cos\theta_d + 1) + \frac{\pi\phi_d^3}{4}(\cos\theta_d - 1)\left(1 + \frac{\cos\theta_d}{2}\right) = 0 . \quad (18)$$

458
 459 It is noted that the semi-empirical results from equations (14) and (16) as well as theoretical results
 460 from equation (18) agree well with the experimental data, as shown in Fig. 4(a) and (b). Since the
 461 droplet evaporation rate depends on the spreading behavior, these relations can be used to predict
 462 the spreading dynamics of the Ag-GNP nanofluid/hybrid nanofluid droplets over their respective
 463 residue surfaces. Fig. 4(c) shows the quasi-equilibrium contact angle (θ_{qe}) and the quasi-
 464 equilibrium contact diameter (ϕ_{qe}) for all considered nanofluid/hybrid nanofluid droplets at
 465 $V_{fd}/V_{sd}=20$. The insets of Fig. 4(c) illustrate the droplet images at a quasi-equilibrium state. It is
 466 observed that both GNP nanofluid and MR-1 hybrid nanofluid droplets show promising wetting
 467 characteristics (low contact angle and large contact diameter) on their highly wetted residue
 468 surfaces, which results in large evaporation rates. However, the wetting properties are adversely
 469 affected (high contact angle and small contact diameter), moving from MR-2 to MR-5 hybrid
 470 nanofluid droplets, while poor wetting is observed for the Ag nanofluid droplet on its highly non-
 471 wetted residue surface, which results in low evaporation rates. The quasi-equilibrium contact angle
 472 and contact diameter for all considered droplets at $V_{fd}/V_{sd}=20$ are correlated by an exponential
 473 function, as shown in Fig. 4(c). Also, the contact angle and contact diameter obtained from
 474 equations (6) and (7) at a quasi-equilibrium state show a good agreement with the experimental
 475 data.

476
 477 Fig. 4(d) shows the effect of the droplet residue size (V_{fd}/V_{sd}) on the quasi-equilibrium contact
 478 angle (θ_{qe}) of the Ag-GNP nanofluid/hybrid nanofluid droplets. It is observed that the GNP
 479 nanofluid and MR-1 hybrid nanofluid droplets completely wet their respective residues, with
 480 $\theta_{qe} \approx 100^\circ$, $\theta_{qe} \approx 41^\circ$, $\theta_{qe} \approx 22^\circ$ for $V_{fd}/V_{sd}=1$, $V_{fd}/V_{sd}=5$ and $V_{fd}/V_{sd}=10$, respectively. However,
 481 the residue at $V_{fd}/V_{sd}=20$ remains partially wetted, despite having a highly wetted surface
 482 ($\theta_{qe} \approx 10^\circ$). It is also noteworthy that the droplets do not spread beyond the residue boundaries,
 483 for $V_{fd}/V_{sd}=1$ to $V_{fd}/V_{sd}=10$, due to the low surface free energy of the Cu surface ($\gamma_{sv} = 33$ mN/m).
 484 This suggests that the droplet wetting characteristics (contact angle and contact diameter) can be
 485 manipulated by its residue size, for cases where the droplets reach up to the residue boundaries.
 486 **Increasing residue size increases droplet spreading on a highly wetted residue surface for GNP**
 487 **nanofluid and MR-1 hybrid nanofluid droplets. This increases the interfacial surface area and the**

488 **droplet evaporation rate.** Moreover, MR-2 and MR-3 hybrid nanofluid droplets completely wet
489 their residues for $V_{fd}/V_{sd}=1$ ($\theta_{qe} \approx 100^\circ$) and $V_{fd}/V_{sd}=5$ ($\theta_{qe} \approx 41^\circ$), while partial wetting is
490 observed for $V_{fd}/V_{sd}=10$ ($\theta_{qe} \approx 26^\circ$) and $V_{fd}/V_{sd}=20$ ($\theta_{qe} \approx 24^\circ$). MR-4 and MR-5 hybrid nanofluids
491 and Ag nanofluid only show complete wetting for $V_{fd}/V_{sd}=1$ ($\theta_{qe} \approx 100^\circ$), while their residues
492 remain partially wetted for $V_{fd}/V_{sd}=5$, $V_{fd}/V_{sd}=10$ and $V_{fd}/V_{sd}=20$. Furthermore, unlike other
493 nanofluid/hybrid nanofluid droplets, the quasi-equilibrium contact angle for the Ag nanofluid
494 droplet increases with increasing values of V_{fd}/V_{sd} . This is because of the increase in surface
495 roughness with residue size (as shown in Table 2), which makes the surface increasingly non-
496 wetted, as the residue size is increased.

497

498 Fig. 5 shows the variation in contact angle and contact diameter, due to the Ag-GNP
499 nanofluid/hybrid nanofluid droplet evaporation on the Cu surface, and their respective residue
500 surfaces, for different values of V_{fd}/V_{sd} . It is noticed that the droplet remains pinned for most part
501 of the droplet evaporation (constant contact diameter), while some depinning is observed near the
502 end of the droplet evaporation, for all considered nanofluid/hybrid nanofluid droplets. The main
503 reason for the pinning effect in the studied droplets is the migration of nanoparticles/hybrid
504 nanoparticles near the three-phase contact line of the evaporating droplet. On the other hand, the
505 contact angle varies with time during the course of the nanofluid/hybrid nanofluid droplet
506 evaporation. It is observed that the contact angle reduction rate is almost the same for all studied
507 droplets, when Cu and residue with $V_{fd}/V_{sd}=1$ are used as substrates. **As both Cu and residue with**
508 **$V_{fd}/V_{sd}=1$ show poor wettability ($\theta_{qe} \approx 100^\circ - 140^\circ$) for all studied droplets, this results in small**
509 **liquid-vapor droplet interfacial areas and subsequently low evaporation rates.** Moreover, the
510 contact angle reduction rate is non-uniform for these cases. On the other hand, the contact angle
511 reduction rate is nearly constant for all nanofluid/hybrid nanofluid droplets (except the Ag
512 nanofluid droplet), when $V_{fd}/V_{sd} \geq 5$. For the Ag nanofluid droplet, evaporation occurs at non-
513 uniform contact angle reduction rates for all V_{fd}/V_{sd} values, due to a highly non-wetted residue
514 surface. In order to understand the underlying mechanisms for wetting transition, from a highly
515 wetted GNP nanofluid/MR-1 hybrid nanofluid droplet residue surface ($\theta_{qe} \approx 10^\circ$) to a highly non-
516 wetted Ag nanofluid droplet residue surface ($\theta_{qe} \approx 142^\circ$), all droplet residues are characterized,
517 as discussed in the next sub-section 4.3.

518

4.3. Droplet Residue Surface Characteristics

The residue surface properties such as the porosity and surface roughness directly affect the droplet evaporation rate. A porous surface with high surface roughness leads to high droplet spreading on its surface and it increases the liquid-air interfacial area and the droplet evaporation rate. The measured data on residue surface properties is shown in Table 2. It is noticed that the mean Feret Diameter (pore size), areal porosity and surface roughness decrease, as we proceed from GNP nanofluid/MR-1 hybrid nanofluid to MR-5 hybrid nanofluid/Ag nanofluid droplet residues. Conversely, the mean Feret Diameter, areal porosity and surface roughness increase with increasing residue size, for each nanofluid/hybrid nanofluid droplet residue. A similar trend is observed for variation in droplet evaporation rate with respect to the mixing ratio and the residue size. This suggests that the evaporation rate of subsequent droplet is affected by the residue surface properties. It must also be noted that the droplet volume (V_{fd}) in Table 2 refers to the volume of the first nanofluid/hybrid nanofluid droplet, which we used to develop the residue on the Cu surface. More details on residue surface properties, such as the residue surface morphology and pore size distribution, can be obtained from supplementary material.

The droplet evaporation rate also depends on the residue surface free energy. The surface free energy of the Cu surface, as well as the Ag-GNP nanofluid/hybrid nanofluid droplet residue surfaces, is shown in Fig. 6. It is observed that the surface free energy decreases, as we move from the GNP nanofluid droplet residue to the Ag nanofluid droplet residue. The surface free energy of each residue is compared with the uncorrected (includes roughness effects) surface free energy, as shown in Fig. 6. It is noticed that the GNP nanofluid and MR-1 hybrid nanofluid droplet residues give the highest uncorrected surface free energy, with large polar components, which results in highly wetted surfaces, and eventually give high evaporation rates for respective droplets residing on these surfaces. However, the surface free energy, as well as its polar component, decrease, as we move from MR-2 to MR-5 hybrid nanofluid droplet residue, and this results in partially wetted surfaces and consequently gives low droplet evaporation rates. The copper surface, and the Ag nanofluid droplet residue surface, both show very low surface free energy values, with negligible polar components, which results in non-wetted surfaces, and gives extremely low evaporation rates for droplets residing on these surfaces.

5. Conclusions

Although droplet evaporation offers high heat transfer rates due to a phase change process, such techniques are still not effective for thermal management of high heat flux devices due to the limiting heat removal capacity of conventional fluids, such as water. To address this issue, we have investigated the droplet evaporation of the Ag-GNP hybrid nanofluid, due to its synergistic thermal properties, for various mixing ratios and residue sizes. As a main novelty of our work, we have shown that the evaporation rate of the subsequent Ag-GNP hybrid nanofluid droplet, resting on its residue surface, varies significantly with varying mixing ratio and residue size. Another novelty lies in a range of wetting behavior, from highly wetted GNP nanofluid and MR-1 hybrid nanofluid droplet residues to an extremely non-wetted Ag nanofluid droplet residue, while having partially wetted MR-2 to MR-5 hybrid nanofluid droplet residues. We also showed that large spreading of GNP nanofluid and MR-1 hybrid nanofluid droplets over their respective wetted residues increases the droplet-air interfacial area and it increases the droplet evaporation rate. Moreover, all residues have a porous structure with varying pore size and areal porosity. Also, the residue surface roughness increases with increasing porosity, which leads to increasing wettability and evaporation rate of the subsequent droplets resting on such residue surfaces. Following are the main conclusions of this study:

- MR-1 hybrid nanofluid droplet gives the highest evaporation rate (370% higher than that of the Ag nanofluid droplet) due to a highly wetted residue surface for $V_{fd}/V_{sd}=20$.
- The evaporation rate is remarkably increased by about 285% as V_{fd}/V_{sd} is increased from 1 to 20 for GNP nanofluid and MR-1 hybrid nanofluid droplets resting on their respective residue surfaces.
- The evaporation rate substantially drops moving from MR-2 to MR-5 hybrid nanofluid droplets, while Ag nanofluid droplets give the least evaporation rates for $V_{fd}/V_{sd}\geq 5$.
- High droplet spreading is achieved in GNP nanofluid and MR-1 hybrid nanofluid droplets, while the droplet spreading is reduced when moving from MR-2 to MR-5 hybrid nanofluid droplets on their respective residue surfaces.
- The quasi-equilibrium contact angle increases from about 10° in GNP nanofluid and MR-1 hybrid nanofluid droplets to about 142° in Ag nanofluid droplets on their respective residue surfaces.

- 581 • The quasi-equilibrium contact angle is reduced from 100° to 10° for GNP nanofluid and
582 MR-1 hybrid nanofluid droplets as V_{fd}/V_{sd} is increased from 1 to 20.
- 583 • The pore size (Feret diameter) and areal porosity increase with increasing residue size,
584 while they decrease with increasing mixing ratios (MR-1 to MR-5) of hybrid nanofluid
585 droplet residues.

586

587 **Acknowledgements**

588 The funding for this research is provided by the Hong Kong PhD Fellowship Scheme (HKPFS),
589 the Hong Kong Research Grant Council via Collaborative Research Fund (CRF) account C6022-
590 16G, General Research Fund (GRF) account 16206918 and Early Career Scheme (ECS) account
591 21200819.

592

593 **References**

- 594 [1] M.A. Ebadian, C.X. Lin, A Review of High-Heat-Flux Heat Removal Technologies, *J. Heat*
595 *Transfer.* 133 (2011). <https://doi.org/10.1115/1.4004340>.
- 596 [2] C.Y. Tso, S.C. Fu, C.Y.H. Chao, A semi-analytical model for the thermal conductivity of
597 nanofluids and determination of the nanolayer thickness, *Int. J. Heat Mass Transf.* 70 (2014)
598 202–214. <https://doi.org/https://doi.org/10.1016/j.ijheatmasstransfer.2013.10.077>.
- 599 [3] S. Fu, C. Tso, Y. Fong, C.Y.H. Chao, Evaporation of Al₂O₃-water nanofluids in an
600 externally micro-grooved evaporator, *Sci. Technol. Built Environ.* 23 (2017) 345–354.
601 <https://doi.org/10.1080/23744731.2016.1250562>.
- 602 [4] C.Y. Tso, C.Y.H. Chao, Study of enthalpy of evaporation, saturated vapor pressure and
603 evaporation rate of aqueous nanofluids, *Int. J. Heat Mass Transf.* 84 (2015) 931–941.
604 <https://doi.org/10.1016/j.ijheatmasstransfer.2015.01.090>.
- 605 [5] F.R. Siddiqui, C.Y. Tso, K.C. Chan, S.C. Fu, C.Y.H. Chao, On trade-off for dispersion
606 stability and thermal transport of Cu-Al₂O₃ hybrid nanofluid for various mixing ratios, *Int.*
607 *J. Heat Mass Transf.* 132 (2019) 1200–1216.
608 <https://doi.org/https://doi.org/10.1016/j.ijheatmasstransfer.2018.12.094>.
- 609 [6] G.M. Moldoveanu, G. Huminic, A.A. Minea, A. Huminic, Experimental study on thermal

- 610 conductivity of stabilized Al₂O₃ and SiO₂ nanofluids and their hybrid, *Int. J. Heat Mass*
611 *Transf.* 127 (2018) 450–457.
612 <https://doi.org/https://doi.org/10.1016/j.ijheatmasstransfer.2018.07.024>.
- 613 [7] S. Suresh, K.P. Venkitaraj, P. Selvakumar, M. Chandrasekar, Synthesis of Al₂O₃–Cu/water
614 hybrid nanofluids using two step method and its thermo physical properties, *Colloids*
615 *Surfaces A Physicochem. Eng. Asp.* 388 (2011) 41–48.
616 <https://doi.org/https://doi.org/10.1016/j.colsurfa.2011.08.005>.
- 617 [8] M.J. Nine, M. Batmunkh, J.-H. Kim, H.-S. Chung, H.-M. Jeong, Investigation of Al₂O₃-
618 MWCNTs Hybrid Dispersion in Water and Their Thermal Characterization, *J. Nanosci.*
619 *Nanotechnol.* 12 (2012) 4553–4559. <https://doi.org/10.1166/jnn.2012.6193>.
- 620 [9] M. Batmunkh, M.R. Tanshen, M.J. Nine, M. Myekhlai, H. Choi, H. Chung, Thermal
621 Conductivity of TiO₂ Nanoparticles Based Aqueous Nanofluids with an Addition of a
622 Modified Silver Particle, *Ind. Eng. Chem. Res.* 53 (2014) 8445–8451.
623 <https://doi.org/10.1021/ie403712f>.
- 624 [10] M.R. Han, Z. H, Yang, B., Kim, S. H., Zachariah, Application of hybrid
625 sphere/carbonnanotube particles in nanofluids, *Nanotechnology.* 18 (2007) 105–109.
- 626 [11] M. Radiom, C. Yang, W.K. Chan, Dynamic contact angle of water-based titanium oxide
627 nanofluid, *Nanoscale Res. Lett.* 8 (2013) 282. <https://doi.org/10.1186/1556-276X-8-282>.
- 628 [12] D. Chakraborty, G.S. Sudha, S. Chakraborty, S. DasGupta, Effect of submicron particles on
629 electrowetting on dielectrics (EWOD) of sessile droplets, *J. Colloid Interface Sci.* 363
630 (2011) 640–645. <https://doi.org/https://doi.org/10.1016/j.jcis.2011.07.077>.
- 631 [13] S.J. Hong, T.H. Chou, Y.Y. Liu, Y.J. Sheng, H.K. Tsao, Advancing and receding wetting
632 behavior of a droplet on a narrow rectangular plane, *Colloid Polym. Sci.* 291 (2013) 347–
633 353. <https://doi.org/10.1007/s00396-012-2797-5>.
- 634 [14] F.R. Siddiqui, C.Y. Tso, S.C. Fu, C.Y.H. Chao, H.H. Qiu, Experimental Investigation On
635 Silver-Graphene Hybrid Nanofluid Droplet Evaporation And Wetting Characteristics Of Its
636 Nanostructured Droplet Residue, in: *ASME-JSME-KSME 2019 8th Jt. Fluids Eng. Conf.*,
637 San Francisco, 2019: pp. 1–8. <https://doi.org/https://doi.org/10.1115/AJKFluids2019-5049>.

- 638 [15] T.A.H. Nguyen, A. V Nguyen, Increased Evaporation Kinetics of Sessile Droplets by Using
639 Nanoparticles, *Langmuir*. 28 (2012) 16725–16728. <https://doi.org/10.1021/la303293w>.
- 640 [16] R.D. Deegan, O. Bakajin, T.F. Dupont, G. Huber, S.R. Nagel, T.A. Witten, Contact line
641 deposits in an evaporating drop, 62 (2000) 756–765.
- 642 [17] R.D. Deegan, Pattern formation in drying drops, *Phys. Rev. E - Stat. Physics, Plasmas,*
643 *Fluids, Relat. Interdiscip. Top.* 61 (2000) 475–485.
644 <https://doi.org/10.1103/PhysRevE.61.475>.
- 645 [18] F.-C. Wang, H.-A. Wu, Pinning and depinning mechanism of the contact line during
646 evaporation of nano-droplets sessile on textured surfaces, *Soft Matter*. 9 (2013) 5703–5709.
647 <https://doi.org/10.1039/C3SM50530H>.
- 648 [19] R. V Craster, O.K. Matar, K. Sefiane, Pinning, Retraction, and Terracing of Evaporating
649 Droplets Containing Nanoparticles, *Langmuir*. 25 (2009) 3601–3609.
650 <https://doi.org/10.1021/la8037704>.
- 651 [20] C. Zhang, X. Zhu, L. Zhou, Morphology tunable pinning force and evaporation modes of
652 water droplets on PDMS spherical cap micron-arrays, *Chem. Phys. Lett.* 508 (2011) 134–
653 138. <https://doi.org/https://doi.org/10.1016/j.cplett.2011.04.041>.
- 654 [21] X. Zhong, A. Crivoi, F. Duan, Sessile nanofluid droplet drying, *Adv. Colloid Interface Sci.*
655 217 (2015) 13–30. <https://doi.org/10.1016/j.cis.2014.12.003>.
- 656 [22] R.D. Deegan, O. Bakajin, T.F. Dupont, G. Huber, S.R. Nagel, T.A. Witten, Capillary flow
657 as the cause of ring stains from dried liquid drops, *Nature*. 389 (1997) 827–829.
658 <https://doi.org/10.1038/39827>.
- 659 [23] K. Sefiane, R. Bennacer, Nanofluids droplets evaporation kinetics and wetting dynamics on
660 rough heated substrates, *Adv. Colloid Interface Sci.* 147–148 (2009) 263–271.
661 <https://doi.org/https://doi.org/10.1016/j.cis.2008.09.011>.
- 662 [24] M. Moghiman, B. Aslani, Influence of nanoparticles on reducing and enhancing evaporation
663 mass transfer and its efficiency, *Int. J. Heat Mass Transf.* 61 (2013) 114–118.
664 <https://doi.org/https://doi.org/10.1016/j.ijheatmasstransfer.2013.01.057>.

- 665 [25] R.-H. Chen, T.X. Phuoc, D. Martello, Effects of nanoparticles on nanofluid droplet
666 evaporation, *Int. J. Heat Mass Transf.* 53 (2010) 3677–3682.
667 <https://doi.org/https://doi.org/10.1016/j.ijheatmasstransfer.2010.04.006>.
- 668 [26] H. Hu, R.G. Larson, Evaporation of a Sessile Droplet on a Substrate, *J. Phys. Chem. B.* 106
669 (2002) 1334–1344. <https://doi.org/10.1021/jp0118322>.
- 670 [27] R.G. Picknett, R. Bexon, The Evaporation of Sessile or Pendant Drops in Still Air, *J. Colloid*
671 *Interface Sci.* 61 (1977) 336–350.
- 672 [28] Y.O. Popov, Evaporative deposition patterns : Spatial dimensions of the deposit, *Phys. Rev.*
673 *E.* 71 (2005) 1–17. <https://doi.org/10.1103/PhysRevE.71.036313>.
- 674 [29] H.H. Lee, S.C. Fu, C.Y. Tso, C.Y.H. Chao, Study of residue patterns of aqueous nanofluid
675 droplets with different particle sizes and concentrations on different substrates, *Int. J. Heat*
676 *Mass Transf.* 105 (2017) 230–236.
677 <https://doi.org/https://doi.org/10.1016/j.ijheatmasstransfer.2016.09.093>.
- 678 [30] P.J. Yunker, T. Still, M.A. Lohr, A.G. Yodh, Suppression of the coffee-ring effect by shape-
679 dependent capillary interactions, *Nature.* 476 (2011) 308–311.
680 <https://doi.org/10.1038/nature10344>.
- 681 [31] T.P. Bigioni, X.-M. Lin, T.T. Nguyen, E.I. Corwin, T.A. Witten, H.M. Jaeger, Kinetically
682 driven self assembly of highly ordered nanoparticle monolayers, *Nat. Mater.* 5 (2006) 265–
683 270. <https://doi.org/10.1038/nmat1611>.
- 684 [32] M. Amjad, Y. Yang, G. Raza, H. Gao, J. Zhang, L. Zhou, X. Du, D. Wen, Deposition pattern
685 and tracer particle motion of evaporating multi-component sessile droplets, *J. Colloid*
686 *Interface Sci.* 506 (2017) 83–92. <https://doi.org/https://doi.org/10.1016/j.jcis.2017.07.025>.
- 687 [33] A. Nikolov, K. Kondiparty, D. Wasan, Nanoparticle Self-Structuring in a Nanofluid Film
688 Spreading on a Solid Surface, *Langmuir.* 26 (2010) 7665–7670.
689 <https://doi.org/10.1021/la100928t>.
- 690 [34] K. Kondiparty, A.D. Nikolov, D. Wasan, K.-L. Liu, Dynamic Spreading of Nanofluids on
691 Solids. Part I: Experimental, *Langmuir.* 28 (2012) 14618–14623.
692 <https://doi.org/10.1021/la3027013>.

- 693 [35] D.T. Wasan, A.D. Nikolov, Spreading of nanofluids on solids, *Nature*. 423 (2003) 156–159.
694 <https://doi.org/10.1038/nature01591>.
- 695 [36] V.M. Starov, M.G. Velarde, C.J. Radke, *Wetting and Spreading Dynamics*, Taylor and
696 Francis, 2007.
- 697 [37] F.R. Siddiqui, C.Y. Tso, K.C. Chan, S.C. Fu, C.Y.H. Chao, Dataset on critical parameters
698 of dispersion stability of Cu/Al₂O₃ nanofluid and hybrid nanofluid for various ultra-
699 sonication times, *Data Br.* 22 (2019) 863–865.
- 700 [38] F.M. Fowkes, Attractive forces at interfaces, *Ind. Eng. Chem.* 56 (1964) 40–52.
701 <https://doi.org/10.1021/ie50660a008>.
- 702 [39] F.P. Incropera, D.P. DeWitt, T.L. Bergman, A.S. Lavine, *Fundamentals of Heat and Mass*
703 *Transfer*, John Wiley and Sons, 2007. <https://doi.org/10.1073/pnas.0703993104>.
- 704 [40] A. Marmur, Soft contact : measurement and interpretation of contact angles, *Soft Matter*. 2
705 (2006) 12–17. <https://doi.org/10.1039/b514811c>.
- 706 [41] T. Young, An Essay on the Cohesion of Fluids, *Philos. Trans. R. Soc. London*. 95 (1805)
707 65–87.
- 708 [42] R.N. Wenzel, Resistance of solid surfaces to wetting by water, *Ind. Eng. Chem.* 28 (1936)
709 988–994. <https://doi.org/10.1021/ie50320a024>.
- 710
- 711

712

713

714

715

716

717 Table 1 Data on roughness ratio, contact angle and interfacial tensions for various droplets and
 718 their respective residues ($V_{fd}/V_{sd}=20$)

Nanofluid/Hybrid Nanofluid	Roughness ratio r	Apparent contact angle θ_a	Surface tension γ_{lv} (mN/m)	Surface free energy γ_{sv} (mN/m)	Solid-liquid interfacial tension γ_{sl} (mN/m)
GNP	1.351±0.143	8.57±0.89	72.433±0.121	56.075±0.274	3.071±0.363
MR-1 0.1(Ag):0.9(GNP)	1.379±0.095	9.49±0.13	68.752±0.130	56.671±0.193	7.523±0.174
MR-2 0.3(Ag):0.7(GNP)	1.305±0.157	26.06±0.06	64.558±0.226	55.138±0.327	10.724±0.298
MR-3 0.5(Ag):0.5(GNP)	1.216±0.073	24.41±0.32	67.812±0.478	60.074±0.217	9.312±0.267
MR-4 0.7(Ag):0.3(GNP)	1.238±0.126	41.44±0.07	63.288±0.172	57.468±0.194	19.173±0.138
MR-5 0.9(Ag):0.1(GNP)	1.191±0.087	52.19±3.08	59.546±0.170	52.291±0.329	21.652±0.327
Ag	1.194±0.138	142.64±0.52	58.927±0.209	43.962±0.285	83.163±0.243

719

720

721

722 Table 2 Surface properties of nanofluid/hybrid nanofluid residues

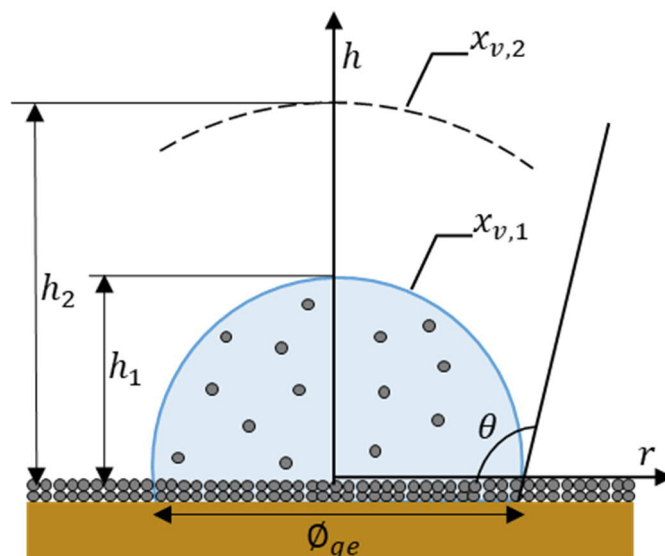
Residue	Droplet Volume $V_{fd}(\mu\text{l})$	Average Roughness $R_a(\mu\text{m})$	Mean Feret Diameter $\phi_f(\mu\text{m})$	Areal Porosity $a_p(\%)$
GNP	3	0.596±0.018	0.742±0.044	4.224±0.204
	15	1.399±0.260	0.751±0.132	23.362±0.632
	30	1.174±0.159	0.703±0.073	24.028±1.145
	60	1.960±0.161	0.740±0.059	24.483±0.655
MR-1	3	0.626±0.094	0.255±0.006	17.157±0.846
	15	1.142±0.228	0.517±0.012	23.702±0.816
	30	1.362±0.223	0.780±0.033	25.826±0.589
	60	2.310±0.212	0.674±0.005	29.017±1.817
MR-2	3	0.977±0.152	0.736±0.015	18.694±1.445
	15	1.510±0.158	0.796±0.006	19.388±0.949
	30	1.747±0.190	0.687±0.078	20.034±1.243
	60	1.826±0.202	0.618±0.027	23.469±0.139
MR-3	3	0.824±0.099	0.695±0.023	14.299±0.260
	15	1.500±0.176	0.786±0.052	19.352±0.870
	30	1.792±0.231	0.753±0.101	21.066±2.226
	60	1.816±0.240	1.026±0.135	26.854±1.549
MR-4	3	0.376±0.100	0.745±0.043	16.193±0.860
	15	1.299±0.157	0.722±0.021	18.918±1.761
	30	1.688±0.197	0.756±0.019	20.404±1.834
	60	1.606±0.201	0.711±0.022	21.006±0.886
MR-5	3	0.322±0.035	0.408±0.008	7.651±0.666
	15	1.303±0.029	0.542±0.018	16.467±0.601
	30	1.574±0.141	0.543±0.024	16.841±0.067
	60	1.604±0.071	0.576±0.022	17.010±0.394
Ag	3	0.127±0.028	0.344±0.017	7.188±0.220
	15	1.038±0.014	0.385±0.048	7.674±0.497
	30	0.598±0.016	0.338±0.017	8.240±0.419
	60	0.914±0.071	0.390±0.004	8.814±0.571

723

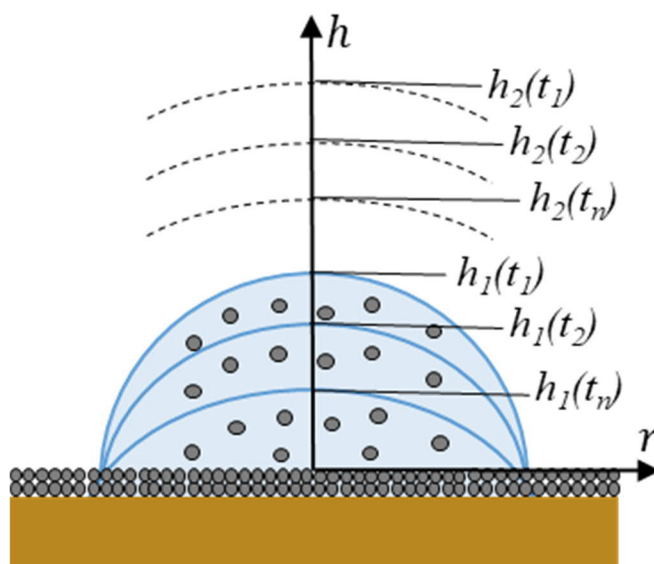
724

725

726



(a)



(b)

727

728

729 Fig. 1 (a) Ag-GNP nanofluid/hybrid nanofluid droplet evaporation over its residue surface. The

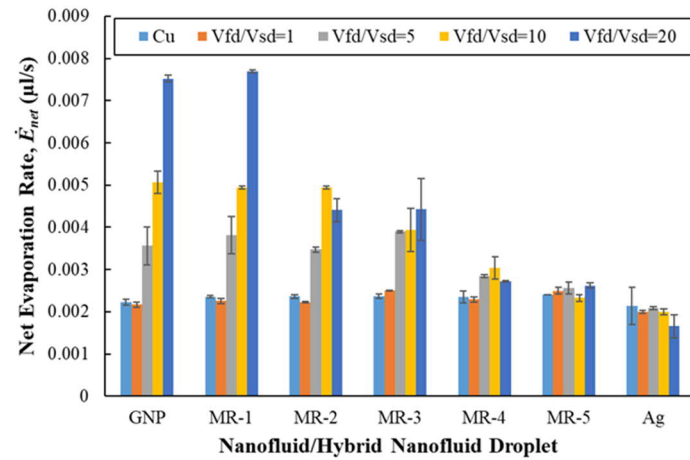
730 suspended nanoparticles (grey balls) in the droplet settle down to form a porous residue surface

731 during the evaporation process, (b) Schematics showing the evaporation of a pinned droplet with

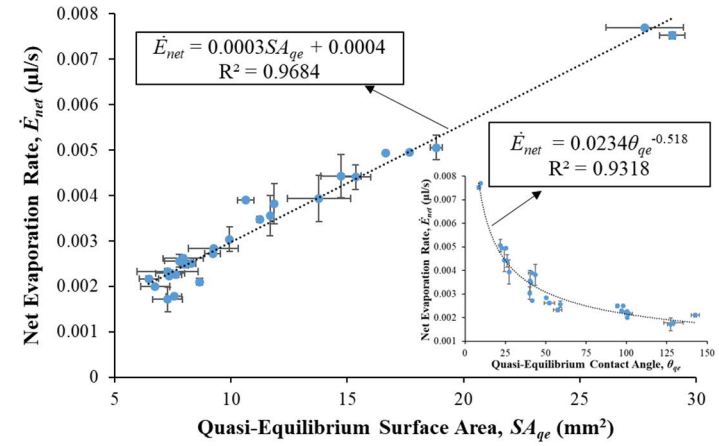
732 varying contact angle over its residue surface over a period of time t_n

733

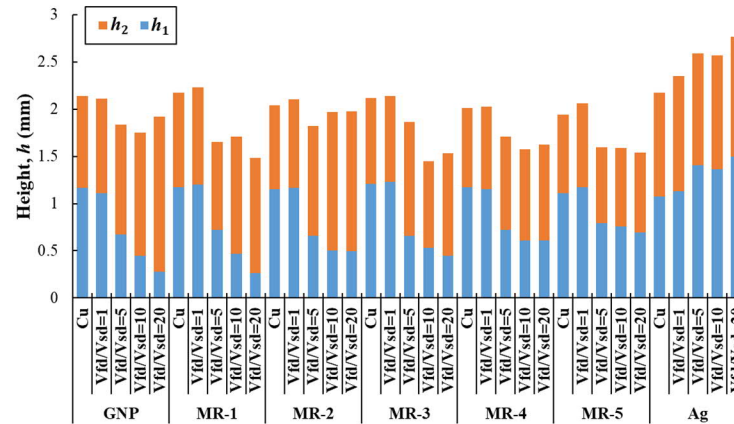
734



(a)

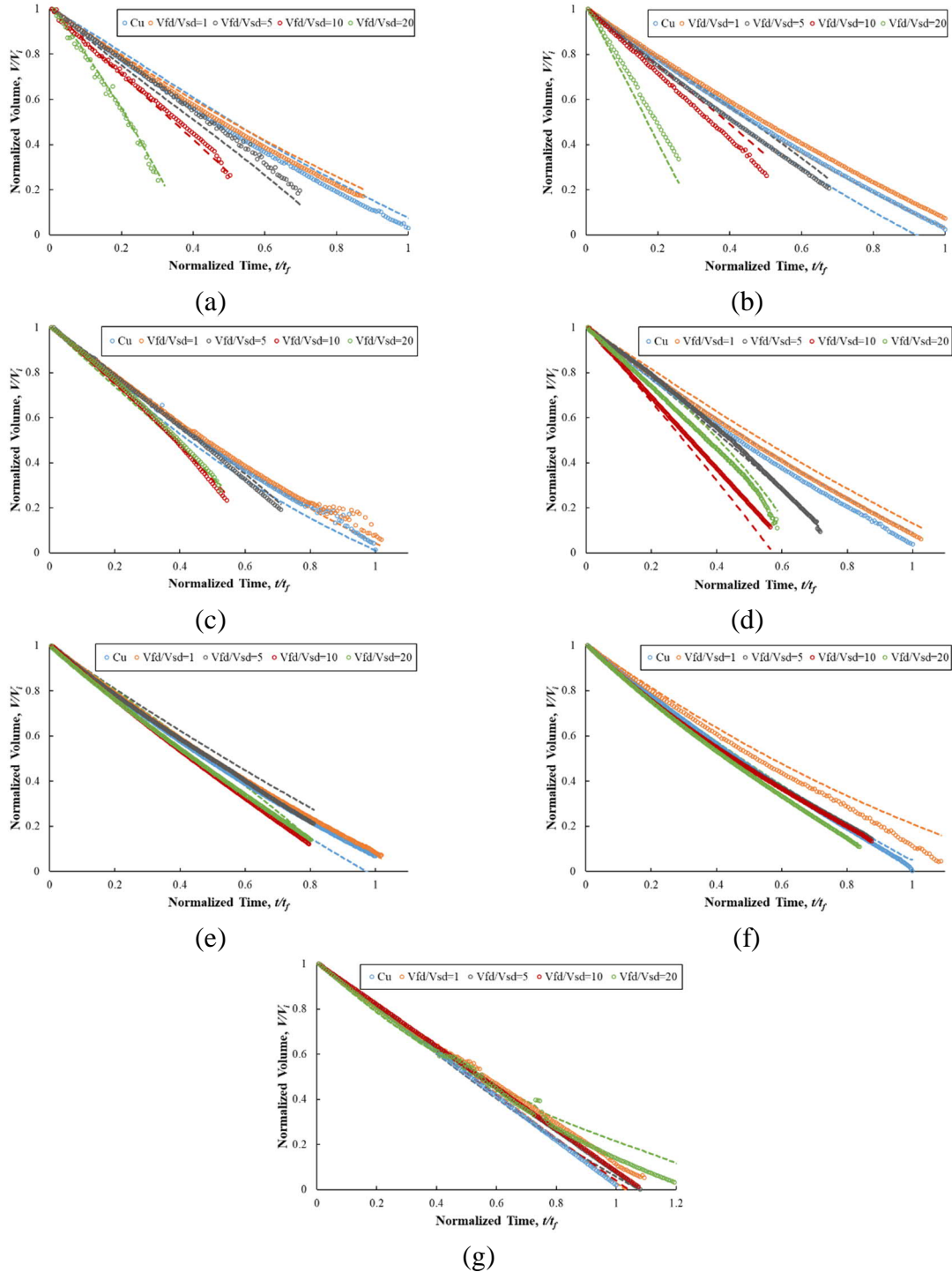


(b)

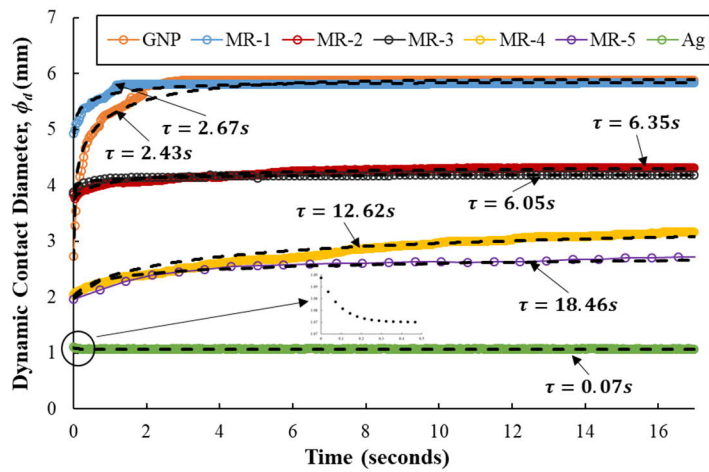


(c)

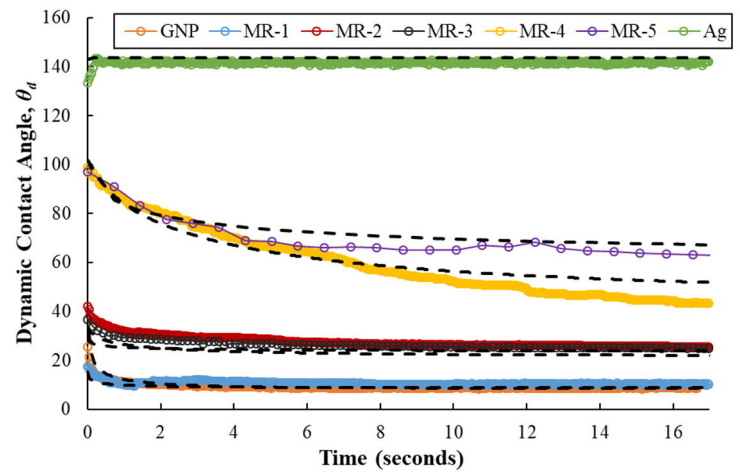
735 Fig. 2 (a) Net evaporation rate of Ag-GNP nanofluid/hybrid nanofluid droplets over Cu surface and their respective residue surfaces,
 736 (b) Net evaporation rate dependence on quasi-equilibrium surface area, (c) Variation of droplet height (h_1) and VES height (h_2) for Ag-
 737 GNP nanofluid/hybrid nanofluid droplets sitting on Cu surface and their respective residue surfaces at quasi-equilibrium state.



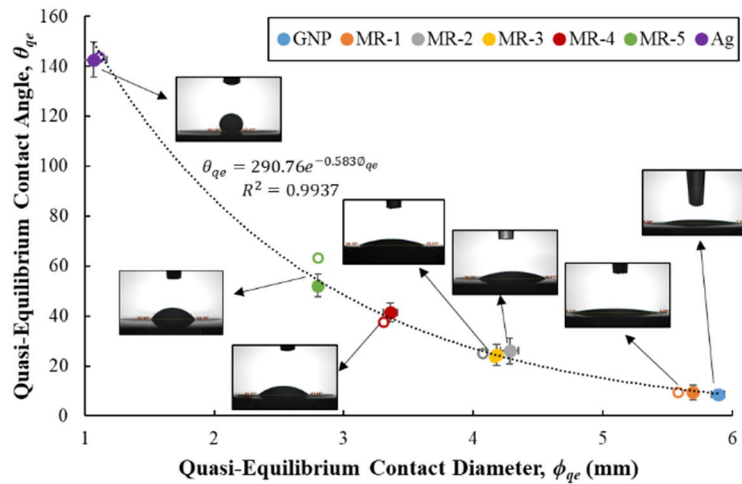
738 Fig. 3 Droplet volume variation with time for (a) GNP nanofluid, (b) MR-1 hybrid nanofluid, (c)
 739 MR-2 hybrid nanofluid, (d) MR-3 hybrid nanofluid, (e) MR-4 hybrid nanofluid, (f) MR-5 hybrid
 740 nanofluid and (g) Ag nanofluid droplets on Cu surface and respective residue surfaces. Unfilled
 741 markers represent the experimental data while dashed lines represent the theoretical result from
 742 equation (4).



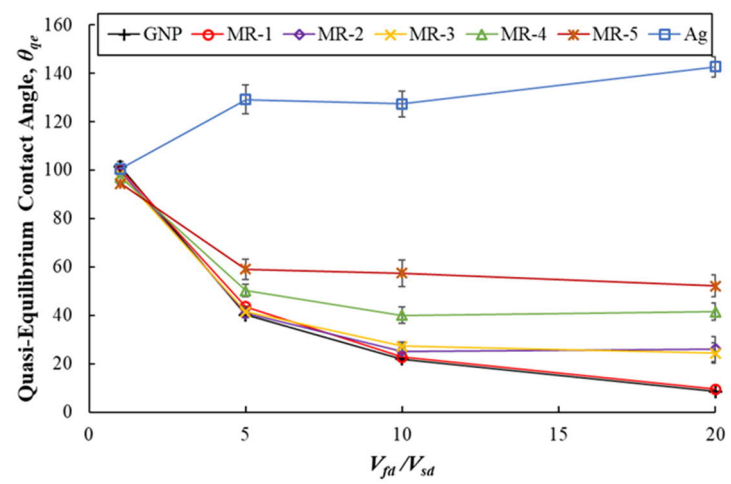
(a)



(b)

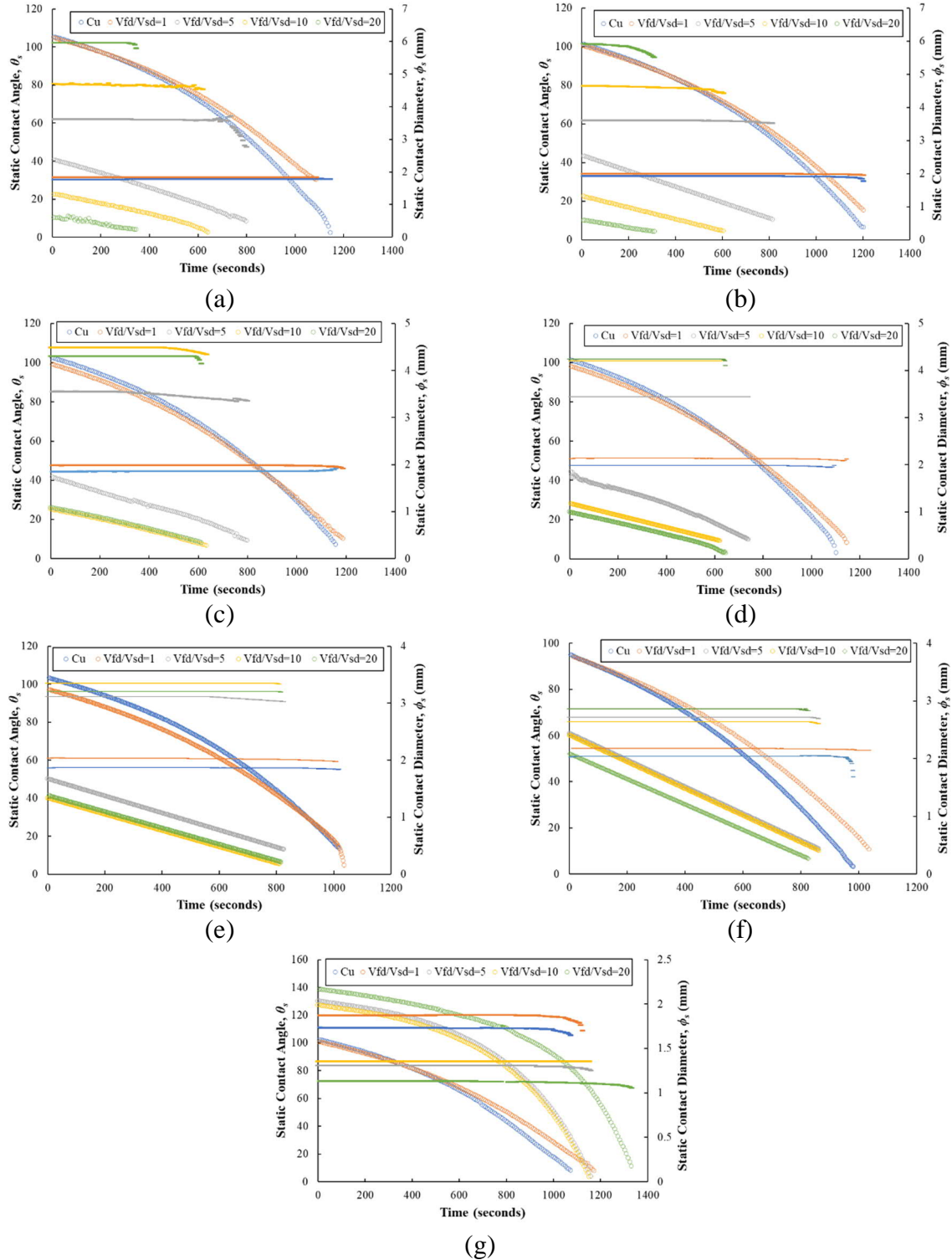


(c)



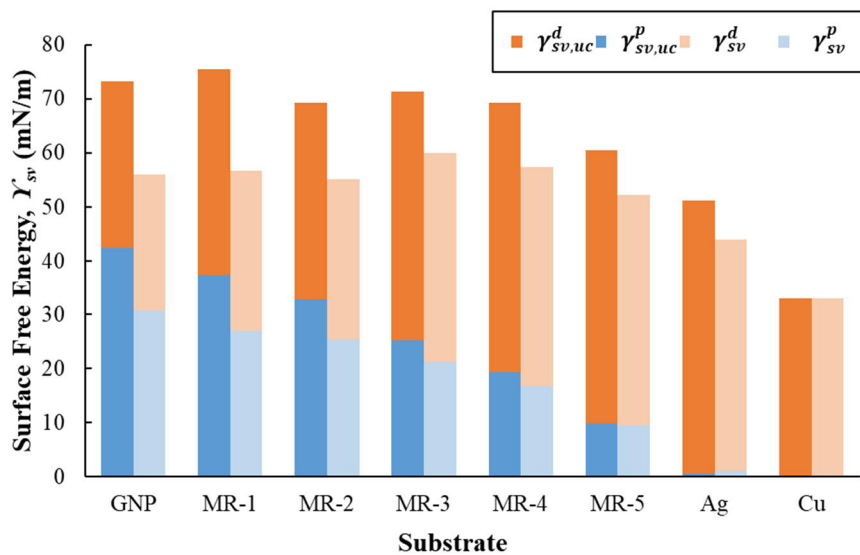
(d)

743 Fig. 4 Nanofluid/hybrid nanofluid droplet spreading over respective residue surfaces showing (a) dynamic contact diameter and (b)
 744 dynamic contact angle with time for $V_{fdl}/V_{sd}=20$. Colored markers represent experimental data and dashed lines represent theoretical
 745 result, (c) Experimental (filled markers) and theoretical (unfilled markers) contact angle and contact diameter at quasi-equilibrium
 746 state for nanofluid/hybrid nanofluid droplets at $V_{fdl}/V_{sd}=20$, (d) Quasi-equilibrium contact angle variation with factor V_{fdl}/V_{sd} .



747 Fig. 5 Static contact angle (unfilled circles) and contact diameter (dashed markers) variation with
 748 time during evaporation for (a) GNP nanofluid, (b) MR-1 hybrid nanofluid, (c) MR-2 hybrid
 749 nanofluid, (d) MR-3 hybrid nanofluid, (e) MR-4 hybrid nanofluid, (f) MR-5 hybrid nanofluid
 750 and (g) Ag nanofluid droplets.

751
752
753
754
755
756



757
758
759
760
761
762
763

Fig. 6 Surface free energy of Cu surface and Ag-GNP nanofluid/hybrid nanofluid droplet residue surfaces. Superscripts p and d represent the polar and dispersive components, while subscript sv,uc represent the roughness uncorrected surface free energy.

Supplementary Material

764
765
766
767
768
769
770
771
772
773
774
775
776
777
778
779
780
781
782
783
784
785
786
787
788
789
790
791

A. Empirical Model for term dx_v/dh

An empirical model is developed for term dx_v/dh pertaining to equation (11) of our main article as a function of the static contact angle (θ_s), mixing ratio (MR) and droplet volume ratio V_{fd}/V_{sd} . The values for MR used in our empirical model are 0, 0.1, 0.3, 0.5, 0.7, 0.9 and 1 for GNP, MR-1, MR-2, MR-3, MR-4, MR-5 and Ag respectively. The values used for V_{fd}/V_{sd} are 0, 1, 5, 10 and 20, where the value 0 corresponds to the droplet resting on a pure copper surface. The developed empirical model contains higher order polynomial terms to fit a large amount of experimental data (6332 data points) and due to the variability in dx_v/dh values with changing θ_s , MR and V_{fd}/V_{sd} values. For this reason, higher order interaction terms are also included in our empirical model to increase the model accuracy. The redundant terms with low coefficient values and p value > 0.05 were removed from the model to obtain a non-hierarchical model while it was ascertained that the model accuracy is not compromised. However, some terms with p value < 0.05, despite having very low coefficient values, were kept in the model as their removal affected the model accuracy. The proposed empirical model is given as:

$$\frac{dx_v}{dh} = a + \sum_{i=1}^n \left[b_i \left(\frac{V_{fd}}{V_{sd}} \right)^i + c_i (MR)^i + d_i (\theta)^i + \sum_{j=1}^k \left(e_{ij} (MR)^i \left(\frac{V_{fd}}{V_{sd}} \right)^j + f_{ij} (\theta)^i \left(\frac{V_{fd}}{V_{sd}} \right)^j + g_{ij} (\theta)^i (MR)^j + \sum_{m=1}^p h_{ijm} \theta^i MR^j \left(\frac{V_{fd}}{V_{sd}} \right)^m \right) \right] \quad (A.1)$$

The coefficient of determination (R^2), the adjusted coefficient of determination (R^2-adj) and the predicted coefficient of determination (R^2-pred) of this model is 94.14%, 94.10% and 93.98% respectively. This suggests that the proposed high fidelity model can be extrapolated to predict dx_v/dh with high level of confidence. Table A.1 shows the coefficient values for all terms used in our model. All coefficient values are used up to the 10 decimal places due to high sensitivity of the proposed model as shown in Table A.1. The residual plots in Fig. A.1 (a) and (b) show that the model fits the experimental data with high accuracy.

792 **B. Residue Morphology and Pore Size Distribution**

793 The SEM micrographs of nanostructured residues, developed by evaporating 60 μl of Ag-GNP
794 nanofluid/hybrid nanofluid droplets over the Cu substrate, are shown in Fig. B.1. It is observed
795 that all residue surfaces have a porous structure, with varying pore size and shapes. Since GNP
796 particles exist in the form of stacked sheets, the pores created by the deposition of GNP particles
797 during the GNP nanofluid droplet evaporation are different in size and shape, as compared to the
798 ones created by the spherical Ag nanoparticles during the Ag nanofluid droplet evaporation. It
799 must also be noted that the residue formed by Ag nanofluid droplet is not uniform (as shown in
800 Fig. B.1 (g)), which indicates possible agglomeration of spherical Ag nanoparticles due to the
801 increased particle concentration during the droplet evaporation process, thus resulting in non-
802 uniform deposition with some large clustered Ag particles in the residue.

803

804 Fig. B.2 shows the pore size distribution for various residue sizes (from $V_{fd} = 3 \mu\text{l}$ to $V_{fd} = 60 \mu\text{l}$) of
805 Ag-GNP nanofluid/hybrid nanofluid droplets. It is observed that a large proportion of pores exist
806 in sub-micron scale, while only a few are above 1 μm size, for all droplet residues. A large
807 proportion of sub-micron pores are even below 0.5 μm in size, as shown in Fig. B.2. It is further
808 noticed that the number of pores above 1 μm size increases, as the residue size is increased (from
809 $V_{fd} = 3 \mu\text{l}$ to $V_{fd} = 60 \mu\text{l}$).

810

811

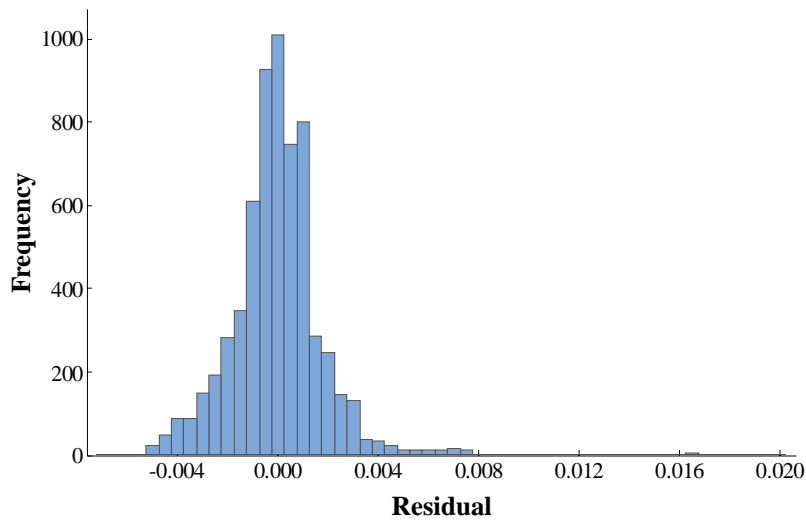
812

813

814 Table A.1 Coefficient values for different terms used in equation (A.1)

Coefficient	Value	Coefficient	Value	Coefficient	Value	Coefficient	Value
a	0.0317573471	c_4	2.5615539109	f_{23}	-	f_{24}	-
b_1	-0.0025278216	d_4	-	g_{23}	-	g_{24}	-0.0000023049
c_1	0.0151831037	e_{13}	0.0013147213	e_{32}	0.0086316105	e_{33}	0.0003042131
d_1	-	f_{13}	0.0000703085	f_{32}	-	f_{33}	-
b_2	0.0006233281	g_{13}	-0.0278015847	g_{32}	-	g_{33}	-
c_2	-0.2498280817	e_{22}	0.0190898913	e_{41}	-	e_{42}	-0.0105948253
d_2	-	f_{22}	-	f_{41}	-	f_{42}	-
e_{11}	0.0399835796	g_{22}	0.0000033475	g_{41}	-	g_{42}	-
f_{11}	-	e_{31}	-0.1472236199	h_{113}	-	e_{51}	0.1057676989
g_{11}	-	f_{31}	-0.0000000072	h_{122}	-0.0000855998	f_{51}	-
b_3	-0.0000732252	g_{31}	-	h_{131}	0.0012069307	g_{51}	-
c_3	-	h_{112}	0.0000095663	h_{212}	-	h_{114}	0.0000000303
d_3	-0.0000000149	h_{121}	0.0004073719	h_{221}	-	h_{123}	-
e_{12}	-0.0139787722	h_{211}	-0.0000035763	h_{311}	-	h_{132}	0.0000549784
f_{12}	-0.0002364804	b_5	-	b_6	-	h_{141}	-0.0012308752
g_{12}	0.0061591758	c_5	-4.4061392885	c_6	2.0923883089	h_{213}	-0.0000000014
e_{21}	-	d_5	-	d_6	-	h_{222}	0.0000000696
f_{21}	0.0000026388	e_{14}	-0.0000349963	e_{15}	-	h_{231}	-
g_{21}	-	f_{14}	-0.0000065444	f_{15}	0.0000001805	h_{312}	-0.0000000001
h_{111}	-0.0001361987	g_{14}	0.0386800317	g_{15}	-0.0172854142	h_{321}	0.0000000106
b_4	0.0000023456	e_{23}	-0.0019666568	e_{24}	0.0000449429	h_{411}	-

815

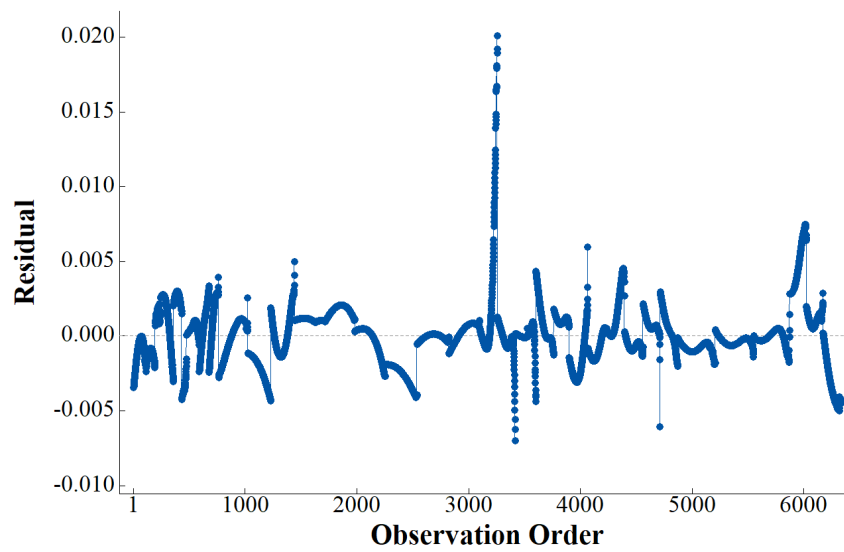


816

817

818

(a)



819

820

(b)

821 Fig. A.1 (a) Histogram of residuals and (b) Residual versus order plot pertaining to the empirical
822 equation (A.1)

823

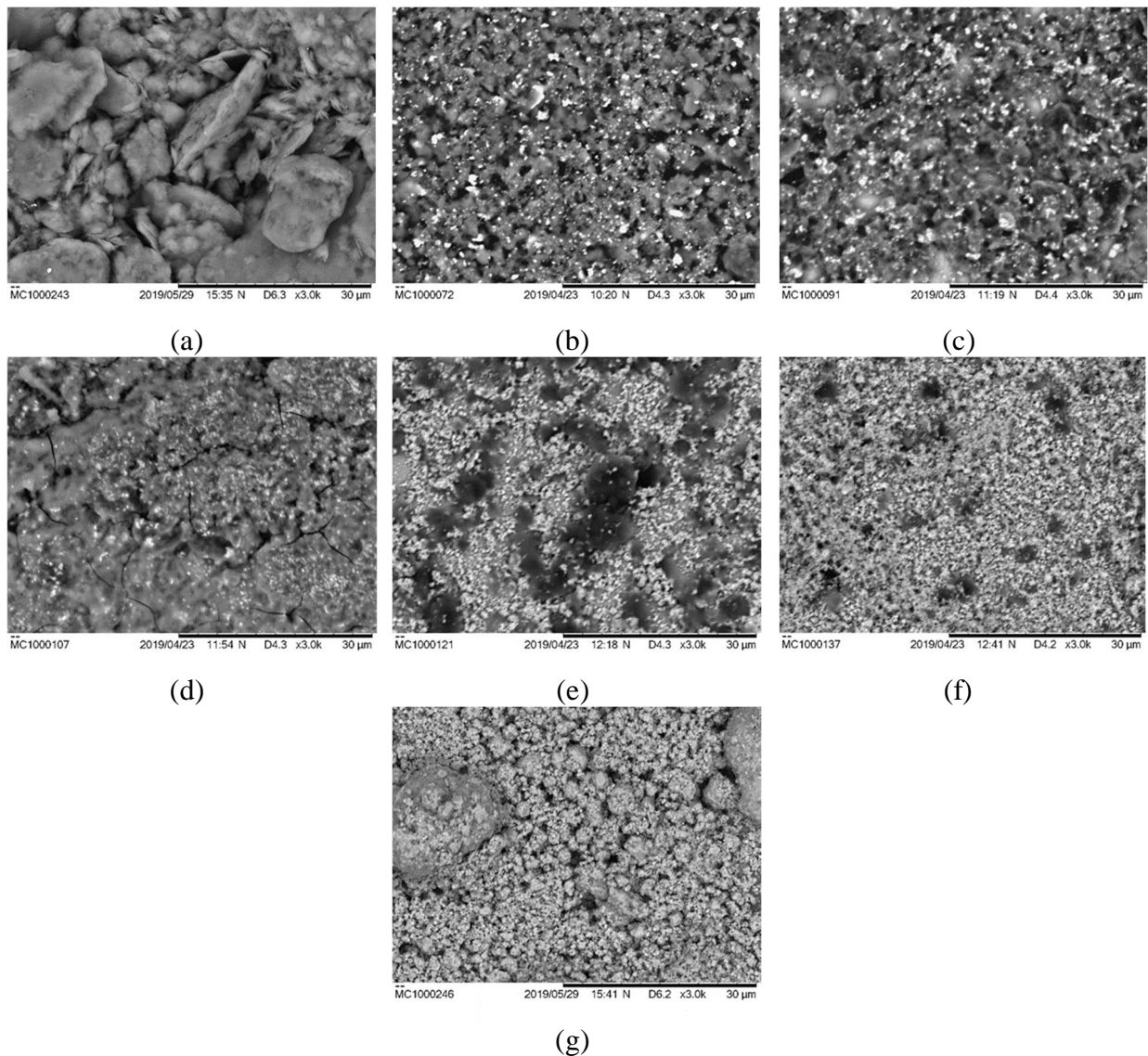
824

825

826

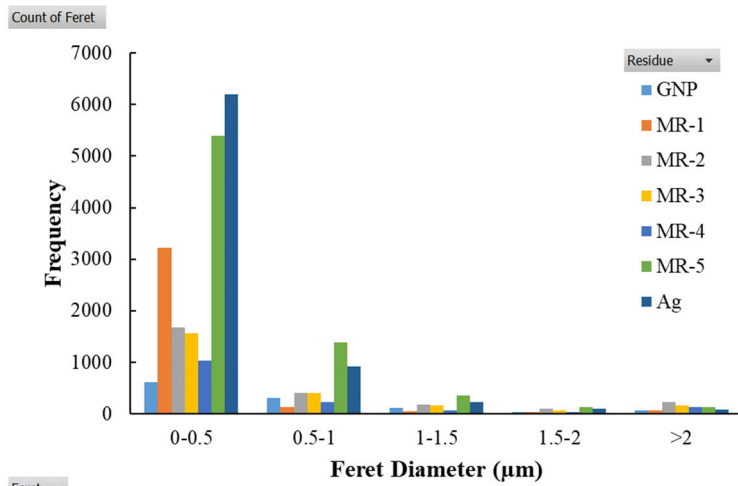
827

828

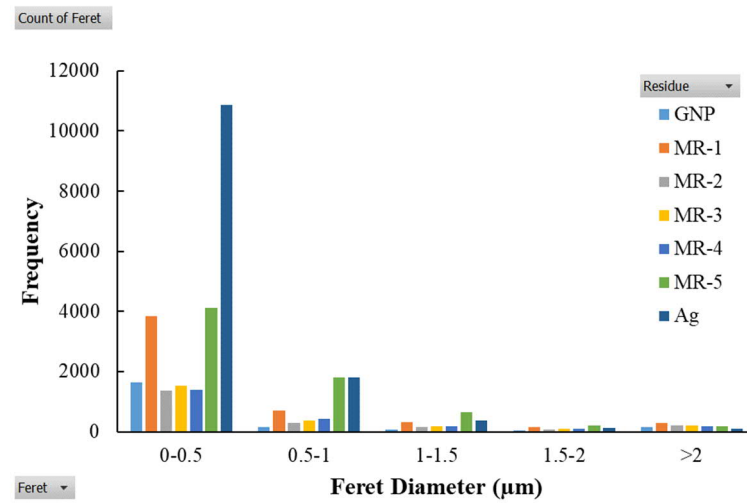


829 Fig. B.1 SEM micrographs of residues developed from 60µl volume of (a) GNP nanofluid, (b)
830 MR-1 hybrid nanofluid, (c) MR-2 hybrid nanofluid, (d) MR-3 hybrid nanofluid, (e) MR-4 hybrid
831 nanofluid, (f) MR-5 hybrid nanofluid and (g) Ag nanofluid droplets on Cu substrate.

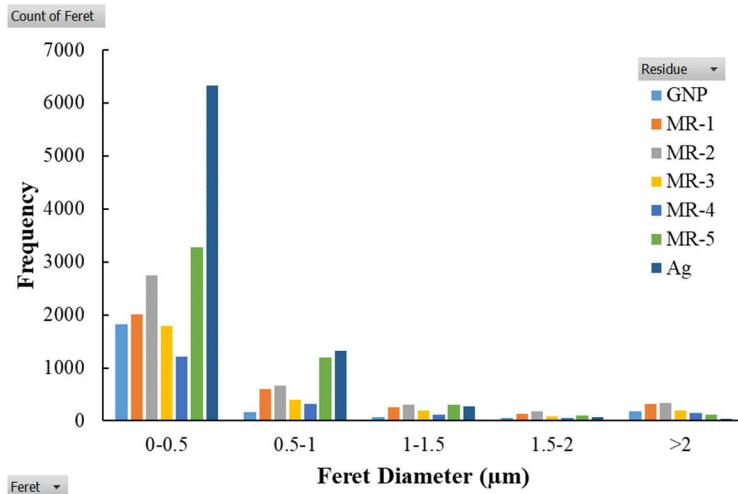
832



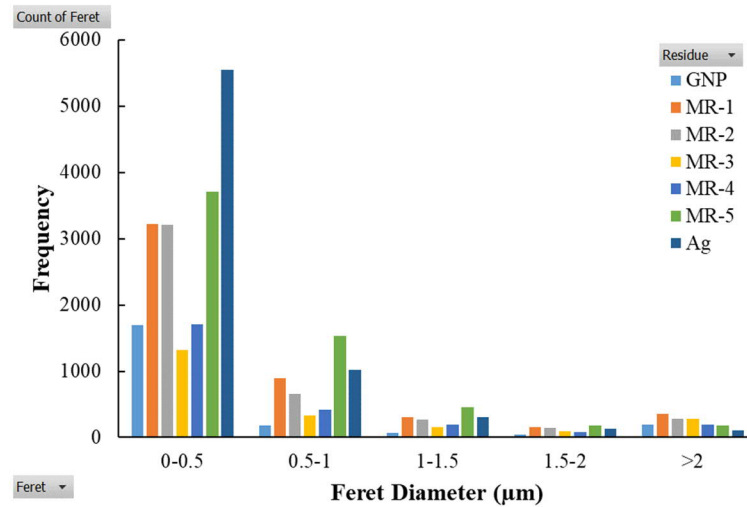
(a)



(b)



(c)



(d)

833 Fig. B.2 Pore size distribution for various mixing ratios of Ag-GNP hybrid nanofluid droplet residue corresponding to (a) $V_{fd} = 3\mu\text{l}$,
 834 (b) $V_{fd} = 15\mu\text{l}$, (c) $V_{fd} = 30\mu\text{l}$ and (d) $V_{fd} = 60\mu\text{l}$.